

SÍGAME Simulations of the [C II], [O I], and [O III] Line Emission from Star-forming Galaxies at $z\simeq 6$

Karen Olsen 1 , Thomas R. Greve 2 , Desika Narayanan 3 , Robert Thompson 4,
Romeel Davé 5,6,7 , Luis Niebla Rios 1, and Stephanie Stawinski 1
School of Earth and Space Exploration, Arizona State University, 781 South Terrace Road, Tempe, AZ 85287, USA; kpolsen@asu.edu
Department of Physics and Astronomy, University College London, Gower Street, London WC1E 6BT, UK
Department of Astronomy, University of Florida, 211 Bryant Space Sciences Center, Gainesville, FL, USA
Portalarium, Austin, TX 78731, USA
Suniversity of the Western Cape, Bellville, Cape Town 7535, South Africa
South African Astronomical Observatory, Observatory, Cape Town 7925, South Africa
Institute for Astronomy, Royal Observatory, Edinburgh EH9 3HJ, UK
Received 2017 May 8; revised 2017 August 10; accepted 2017 August 13; published 2017 September 7

Abstract

Of the almost 40 star-forming galaxies at $z \gtrsim 5$ (not counting quasi-stellar objects) observed in [C II] to date, nearly half are either very faint in [C II] or not detected at all, and fall well below expectations based on locally derived relations between star formation rate and [C II] luminosity. This has raised questions as to how reliable [C II] is as a tracer of star formation activity at these epochs and how factors such as metallicity might affect the [C II] emission. Combining cosmological zoom simulations of galaxies with SÍGAME (SImulator of GAlaxy Millimeter/ submillimeter Emission), we modeled the multiphased interstellar medium (ISM) and its emission in [C II], as well as in [O I] and [O III], from 30 main-sequence galaxies at $z \simeq 6$ with star formation rates $\sim 3-23~M_{\odot}~\rm yr^{-1}$, stellar masses $\sim (0.7-8) \times 10^9 M_{\odot}$, and metallicities $\sim (0.1-0.4) \times Z_{\odot}$. The simulations are able to reproduce the aforementioned [C II] faintness of some normal star-forming galaxy sources at $z \ge 5$. In terms of [O II] and [O III], very few observations are available at $z \gtrsim 5$, but our simulations match two of the three existing $z \gtrsim 5$ detections of [O III] and are furthermore roughly consistent with the [O I] and [O III] luminosity relations with star formation rate observed for local starburst galaxies. We find that the [C II] emission is dominated by the diffuse ionized gas phase and molecular clouds, which on average contribute \sim 66% and \sim 27%, respectively. The molecular gas, which constitutes only $\sim 10\%$ of the total gas mass, is thus a more efficient emitter of [C II] than the ionized gas, which makes up \sim 85% of the total gas mass. A principal component analysis shows that the [C II] luminosity correlates with the star formation activity of a galaxy as well as its average metallicity. The low metallicities of our simulations together with their low molecular gas mass fractions can account for their [C II] faintness, and we suggest that these factors may also be responsible for the [C II]-faint normal galaxies observed at these early epochs.

Key words: cosmology: theory – galaxies: high-redshift – galaxies: ISM – line: formation – methods: numerical – submillimeter: ISM

Supporting material: machine-readable table

1. Introduction

The far-IR (FIR) fine-structure transitions [C II] ${}^{2}P_{3/2} - {}^{2}P_{1/2}$ at 157.7 μ m, [O I] ${}^{3}P_{2} - {}^{3}P_{1}$ at 63.2 μ m, and [O III] ${}^{3}P_{1} - {}^{3}P_{0}$ at 88.4 μ m (hereafter referred to as [C II], [O I], and [O III]) have been used as diagnostic tracers of the interstellar medium (ISM) and star formation activity for over two decades (e.g., Malhotra et al. 1997; Luhman et al. 1998; Fischer et al. 1999; Luhman et al. 2003; Ferkinhoff et al. 2010; Stacey et al. 2010; Sturm et al. 2010; Díaz-Santos et al. 2013; Wang et al. 2013; De Looze et al. 2014; Pineda et al. 2014; Rigopoulou et al. 2014; Sargsyan et al. 2014; Capak et al. 2015; Gullberg et al. 2015; Willott et al. 2015; Diaz-Santos et al. 2017). [C II] is often observed to be one of the strongest emission lines in the spectra of galaxies and can compose up to $\sim 0.1\%$ –1% of the infrared (IR) luminosity (Stacey et al. 1991; Helou et al. 2001). With C⁰ having an ionization potential of only 11.3 eV and with the [C II] line having an upperstate energy of $E_{\rm u}/k_{\rm B}\sim 91$ K, several ISM phases can contribute to its emission. It is an important coolant in diffuse HI clouds, diffuse ionized gas, and even molecular gas, where its critical density spans a wide range from $\sim 5 \text{ cm}^{-3}$ for collisions with electrons at $T_{\rm k}=8000~{\rm K}$ to $\sim 7.6\times 10^3~{\rm cm}^{-3}$ for collisions with molecules at $T_{\rm k}=20~{\rm K}$ (Goldsmith et al. 2012). In photo-dissociation regions (PDRs), it is associated with both the interface layer of atomic gas, as well as from the ionized gas in the HII region itself (e.g., Stacey et al. 1991; Malhotra et al. 2001; Brauher et al. 2008; Smith et al. 2017). [O I] has a critical density of $\sim 4.7\times 10^5~{\rm cm}^{-3}$ and an upper-state energy of $E_{\rm u}/k_{\rm B}\sim 228~{\rm K}$, which makes it an efficient tracer of PDRs. Since the ionization potential of O⁺ is 35.1 eV, [O III] is seen in hot diffuse ionized gas (e.g., HII regions or the hot ionized medium), where the transition is easily excited $(n_{\rm cr}\sim 5.1\times 10^2~{\rm cm}^{-3}$ and $E_{\rm u}/k_{\rm B}\sim 163~{\rm K})$.

Although they trace different ISM phases, all three fine-structure lines have been proposed to be tracers of the star formation rate (SFR) of galaxies (Kapala et al. 2015; Herrera-Camus et al. 2015). For example, De Looze et al. (2014) found the line emissions to correlate with the SFRs for a sample of local and high-z starburst galaxies. However, the same study also found that for local metal-poor dwarfs, [O I] and [O III] were better at predicting the SFR than [C II], which showed an

increased scatter and a somewhat shallower correlation (De Looze et al. 2014). Furthermore, local (ultra) luminous IR galaxies ((U)LIRGs) show a significant decrement in their [C II] luminosity (e.g., Malhotra et al. 2001). Self-absorption of the [O I] line due to intervening cold or subthermally excited gas has also been reported in (U)LIRGS (e.g., Rosenberg et al. 2015), possibly decreasing the line strength and its ability to trace the star formation.

At redshifts >5, [C II] has been detected in little more than a dozen normal star-forming galaxies (Capak et al. 2015; Gullberg et al. 2015; Willott et al. 2015; Knudsen et al. 2016; Pentericci et al. 2016; Bradač et al. 2017; Decarli et al. 2017; Smit et al. 2017), and about the same number of non-detections (i.e., upper limits). The non-detections, and a small number of detections, predominantly have very low $L_{\rm [C\ II]}/{\rm SFR}$ ratios and do not appear to form a [C II]-SFR sequence with the remaining [C II]-detected galaxies (Kanekar et al. 2013; Ouchi et al. 2013; González-López et al. 2014; Ota et al. 2014; Maiolino et al. 2015; Schaerer et al. 2015; Inoue et al. 2016). Proposed explanations for the low [C II] emission include low metallicities and thus C abundance, strong stellar feedback disrupting the neutral ISM from which most [C II] emission is expected to arise (Maiolino et al. 2015; Inoue et al. 2016; Pentericci et al. 2016; Bradač et al. 2017), and extreme UV fields and thus a high ionization parameter $\langle U \rangle^8$ (Willott et al. 2015). An increase in $\langle U \rangle$ leads to higher grain charges (and grain temperatures), causing a deficiency of photoelectrons available to heat the gas and hence a reduced photoelectric heating efficiency. Additionally, the effects of stellar age (González-López et al. 2014; Schaerer et al. 2015) and (possibly much denser) PDR structures different from those seen locally (Ouchi et al. 2013; Ota et al. 2014) have been invoked.

With the low number of [O I] and [O III] detections at high redshift, it is practically impossible to establish an [O I]–SFR or [O III]–SFR relation for the high-redshift (0.5 < z < 6.6) sample of De Looze et al. (2014). Since that study, two Ly α emitters (LAEs) at z=7.2120 and 8.38, and a normal star-forming galaxy at z=7.1 have been detected in [O III] (Inoue et al. 2016; Carniani et al. 2017; Laporte et al. 2017).

Galaxy-scale simulations that attempt to account for the observations of the above fine-structure lines have been developed, in particular, how their emissions are linked to the ISM phases and to global galaxy properties, such as metallicity, star formation efficiency, ionization parameter, dust mass fraction, and compactness and phase-filling factors (e.g., Cormier et al. 2012; Vallini et al. 2013; Olsen et al. 2015; Accurso et al. 2017; Katz et al. 2017). By combining codes of stellar population synthesis, radiative transfer, photoionization, and astrochemistry into simulations of starburst regions, Accurso et al. (2017) found that the increases in the specific star formation rate of a galaxy leads to a decrease in the fraction of the [C II] emission coming from the molecular gas phase, due to stronger UV radiation fields, which will tend to shrink the molecular regions. Applied to local normal galaxies, their code predicts that as much as 60%-80% of the [C II] emission emerges from the molecular gas. Cormier et al. (2012) utilized the photoionization code CLOUDY (Ferland et al. 2013) to model a number of FIR fine-structure line emissions (including [CII], [OI], and [OIII]) from the multiphased ISM in the starburst low-metallicity galaxy Haro 11. They found that

Some simulation studies have focused specifically on $z \gtrsim 6$ galaxies using either cosmological simulations (Vallini et al. 2013, 2015; Pallottini et al. 2017) or an analytical framework (Bonato et al. 2014; Muñoz & Furlanetto 2014; Popping et al. 2016; Narayanan & Krumholz 2017). Simulating galaxies at $z \approx 6.6$, Vallini et al. (2015) parametrized their [C II] luminosities as a function of SFR and metallicity. They find that the [C II]-faint sources at these epochs are explained by either low metallicity or negative feedback from regions of intense star formation. They also find that the [C II] budget is dominated by emission from PDRs, with <10% coming from the diffuse neutral gas. Pallottini et al. (2017) calculated the [C II] emission from a multiphase ISM in a normal star-forming galaxy at $z \simeq 6$ by combining abundance calculations using CLOUDY with the method of inferring the [C II] emission by Vallini et al. (2013, 2015) and applying it to a cosmological simulation. They too were able to reproduce the underluminous [C II] sources found at this epoch and, just like Vallini et al. (2015), attributed it to low metallicity. They also find that while \sim 95% of the total [C II] luminosity is coming from the main gas disk of the galaxy, about 30% of the total C⁺ mass is situated in an outflow. Owing to the low density of the outflow, however, this mass does not contribute significantly to the total [C II] luminosity.

In this paper, we simulate the [C II], [O I], and [O III] line emission from normal star-forming galaxies at $z \simeq 6$, although the emphasis of our analysis will be on [C II]. Due to the different origins of the lines, a multiphased modeling of the ISM is required. To this end, we combined the output from cosmological zoom simulations of normal star-forming galaxies at this epoch with an updated version of SÍGAME (SÍmulator of GAlaxy Millimeter/submillimeter Emission; Olsen et al. 2015). Section 2 describes the simulation codes used for the galaxy evolution and the galaxy sample chosen for our study. The subgrid modeling of the ISM is done with SÍGAME and is described in Section 3. The simulation results are presented, and analyzed and discussed in Section 4 and Section 5, respectively, followed by our conclusions in Section 6. Throughout, we adopt a flat cold dark matter (Λ CDM) cosmology with cosmological parameters $\Omega_{\Lambda} = 0.7$, $\Omega_{\rm M}=0.3$, and h=0.68 (Planck Collaboration et al. 2016).

2. Cosmological Galaxy Formation Simulations

We use cosmological zoom simulations of galaxies extracted from the MUFASA cosmological simulation (Davé et al. 2016, 2017), utilizing the same feedback prescription as in MUFASA. We first briefly summarize the zoom technique, then discuss the particulars of the MUFASA simulations.

The zoom technique has been summarized in recent reviews (e.g., Somerville & Davé 2015), hence we only condense the salient details here. We begin by simulating a dark matter only $50 \, \mathrm{h^{-1} \, Mpc^3}$ volume utilizing GIZMO, which employs the GADGET-2 tree-particle-mesh gravity solver (Springel 2005). This is run at a fairly low resolution, with 512^3 particles resulting in a particle mass of $m_{\mathrm{DM}} = 7.8 \times 10^8 \, h^{-1} \, M_{\odot}$, from z = 249 to z = 0 with the aim of simulating a population of

PDRs account for only 10% of the [C II] emission, with the remaining emission arising in the diffuse ionized medium, but a larger PDR contribution when lowering the density or including magnetic fields.

Number of far-UV photons per hydrogen atom.

⁹ http://www.tapir.caltech.edu/~phopkins/Site/GIZMO.html

dark matter halos to be resimulated (with baryons) at a much higher mass resolution. The initial conditions are generated with MUSIC(Hahn & Abel 2011) and have the exact same random seeds as the cosmological MUFASA simulation with gas dynamics.

At z=2, we identify a randomly selected set of halos within the mass range $\sim (0.4-3) \times 10^{13} \, M_{\odot}$ for resimulation at higher resolution, now including baryons. We build an elliptical mask around each halo extending to $2.5 \times$ the distance of the farthest dark matter particle from the center of the halo, and define this as the Lagrangian high-resolution region to be resimulated. We seed this region with higher-resolution dark matter ($m_{\rm DM}=1\times10^6\,h^{-1}\,M_{\odot}$) and gas $(1.9\times10^5\,h^{-1}\,M_{\odot})$ fluid elements and resimulate. We employ adaptive gravitational softening of all particles throughout the simulation (Hopkins 2015), with minimum force softening lengths of 12, 3, and 3 pc for dark matter, gas, and stars respectively.

The hydrodynamic simulations are run with a modified version of the *N*-body/hydrodynamics solver, GIZMO (Hopkins 2015), using the meshless finite mass (MFM) hydrodynamics solver. MFM uses a Riemann solver to compute pressure gradients, whose solution is obtained in a frame chosen to conserve mass within each mesh cell. This retains the essential advantages of mesh methods that handle shocks and contact discontinuities accurately, along with that of particle-based methods in which mass can be tracked and followed.

These simulations utilize the suite of physics developed for the MUFASA cosmological simulations as described in Davé et al. (2016, 2017). We refer the reader to these papers for more details and summarize the relevant details here. Star formation occurs only in dense molecular gas, where the H_2 gas fraction (f_{H_2}) is determined based on the Krumholz et al. (2009) and Krumholz & Gnedin (2011) relations that approximate the molecular gas mass fraction as a function of the gas-phase metallicity and surface density. Due to our high resolution, we assume no clumping on scales below our resolution limit. Star formation follows a volumetric Schmidt (1959) relation with an imposed star formation efficiency of $\sigma_* = 0.02$.

Young stars generate winds using a decoupled, two-phase wind. These winds have a probability for ejection that is a fraction of the star formation rate probability, according to the best-fit relation from the Feedback in Realistic Environments (FIRE) simulations studied by Muratov et al. (2015; and is additionally motivated by analytic arguments; Hayward & Smith 2015). The ejection velocity scales with the galaxy circular velocity again following the Muratov et al. (2015) scaling relations. These winds are decoupled from hydrodynamic forces or cooling until either its velocity relative to the background gas is less than half the local sound speed; the wind reaches a density limit less than $0.01 \times$ that of the critical density of star formation; or at least 2% of the Hubble time has elapsed since the time of launch.

Feedback from longer-lived stars (i.e., Asymptotic Giant Branch stars and Type Ia supernovae) is also included. These delayed feedback sources follow the Bruzual & Charlot (2003) tracks with a Chabrier (2003) initial mass function, and deposit heavy metals (H, He, C, N, O, Ne, Mg, Si, S, Ca, and Fe) into the ISM. The chemical enrichment yields for Type II SNe, Type Ia SNe, and AGB stars are taken from the Nomoto et al. (2006), Iwamoto et al. (1999), and Oppenheimer & Davé (2008) parameterizations respectively.

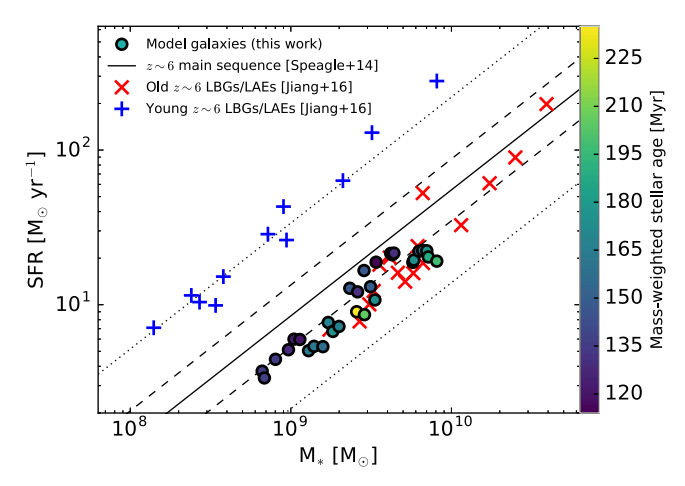


Figure 1. SFR vs. M_* for our 30 simulated galaxies (filled circles, color-coded according to their stellar-mass-weighted average ages). The observed SFR- M_* relation at $z \simeq 6$ as determined by Speagle et al. (2014) is shown as a solid line accompanied by dashed and dotted lines indicating the 1σ and 3σ scatter around the relation, respectively. For comparison, we show the positions of $z \sim 6$ "old" (>100 Myr) and "young" (<30 Myr) LBGs/LAEs (Jiang et al. 2016).

We extract model galaxies from snapshots at 5.875 < z < 6.125 with stellar masses (M_*) and SFRs in the range $\sim (0.7-8) \times 10^9 \, M_{\odot}$ and $\sim 3-23 \, M_{\odot} \, \mathrm{yr}^{-1}$, respectively. In total, we select 30 galaxies, hereafter named G1, ..., G30 in order of increasing stellar mass. Figure 1 shows the locations of G1, ..., G30 in the SFR- M_* diagram. The galaxies are consistent with the observational determination of the $z\sim6$ main sequence (MS) of star-forming galaxies by Speagle et al. (2014), although slightly offset toward higher M_* for a given SFR. Also shown in Figure 1 are the $z \sim 6$ LBGs and LAEs studied by Jiang et al. (2016) who divided their sample into "old" (>100 Myr) and "young" (<30 Myr) galaxies, depending on their stellar age as derived from spectral energy distribution (SED) fitting. As the color-coding shows, our model galaxies are consistent in terms of M_* , SFR, and stellar age with the "old" LBG/LAE population (Jiang et al. 2016). Table 1 gives an overview of the other global parameters of our simulations that are relevant for this study. The SFR of each galaxy was calculated as a mean over the past 100 Myr (mass of new stars created over the past 100 Myr divided by 100 Myr), and the radius of the disk is calculated using the analysis software CAESAR, ¹⁰ an extension of the YT simulation tools, 11 using a friends-of-friends algorithm. Table 1 also lists the average metallicity of each simulated galaxy, which is calculated as the SFR-weighted average over all of the fluid elements. These SFR-weighted average metallicities, $\langle Z \rangle_{SFR}$, range from 14% to 45% of the solar metallicity.

3. SÍGAME

For the purposes of this paper, we updated SÍGAME from the version presented in Olsen et al. (2015). The main updates are a more sophisticated calculation of the UV radiation fields and the implementation of CLOUDY¹² version 17 (Ferland et al. 2017). Below we describe in detail the updates made. Figure 2

¹⁰ https://bitbucket.org/rthompson/caesar

¹¹ http://yt-project.org/

¹² http://www.nublado.org/

Table 1
Global Properties of the 30 Simulated $z \simeq 6$ Galaxies Used for This Work

Name	z	R _{gal} a (kpc)	$M_* (10^9 M_{\odot})$	$M_{\rm gas}~(10^9M_\odot)$	$SFR^b (M_{\odot} yr^{-1})$	$\langle Z \rangle_{ m SFR} ^{ m c} (Z_{\odot})$	$\frac{M_{\rm GMC}}{M_{\rm gas}}$	Mdiffuse neutral Mgas	$\frac{M_{ m diffuse\ ionized}}{M_{ m gas}}$
G1	6.12	9.34	0.663	11.493	3.720	0.186	0.071	0.059	0.869
G2	6.25	7.45	0.684	8.170	3.365	0.136	0.093	0.063	0.844
G3	6.00	8.12	0.802	11.810	4.437	0.178	0.089	0.077	0.833
G4	5.88	9.67	0.967	11.821	5.118	0.183	0.075	0.054	0.871
G5	5.88	8.86	1.047	13.016	5.991	0.170	0.140	0.099	0.761
G6	5.75	7.49	1.138	10.259	5.959	0.152	0.115	0.090	0.794
G7	6.00	9.25	1.289	11.499	5.045	0.156	0.089	0.079	0.831
G8	6.12	11.29	1.393	14.489	5.384	0.155	0.088	0.064	0.847
G9	6.25	8.31	1.583	9.170	5.358	0.198	0.143	0.059	0.797
G10	6.25	5.70	1.710	9.532	7.681	0.159	0.216	0.030	0.754
G11	5.75	12.68	1.826	16.511	6.719	0.236	0.063	0.054	0.882
G12	5.88	11.37	1.994	15.293	7.239	0.211	0.020	0.119	0.861
G13	6.12	7.41	2.329	10.718	12.776	0.208	0.107	0.022	0.871
G14	5.75	11.05	2.569	14.296	9.014	0.231	0.103	0.062	0.835
G15	6.00	9.07	2.603	12.520	12.115	0.242	0.053	0.107	0.840
G16	6.00	7.70	2.856	11.051	16.644	0.202	0.180	0.022	0.798
G17	5.88	6.67	2.873	8.119	8.625	0.258	0.214	0.070	0.716
G18	5.75	13.84	3.134	19.713	13.078	0.217	0.020	0.090	0.889
G19	6.12	10.46	3.338	10.771	10.739	0.282	0.023	0.129	0.848
G20	6.25	7.78	3.395	10.299	18.833	0.334	0.021	0.025	0.954
G21	6.00	4.15	4.186	7.822	21.474	0.412	0.072	0.032	0.896
G22	6.12	6.40	4.277	9.044	21.042	0.452	0.020	0.033	0.947
G23	6.25	6.70	4.381	10.061	21.558	0.339	0.031	0.028	0.941
G24	6.25	7.47	5.750	11.261	18.776	0.293	0.157	0.014	0.828
G25	5.88	7.03	5.833	9.567	19.442	0.354	0.039	0.038	0.923
G26	6.12	10.43	6.278	14.223	22.182	0.371	0.138	0.056	0.805
G27	6.00	10.84	6.622	13.159	22.455	0.370	0.103	0.052	0.844
G28	5.88	10.52	7.024	9.680	22.332	0.425	0.139	0.046	0.815
G29	5.75	7.38	7.178	6.710	20.364	0.392	0.201	0.013	0.785
G30	5.75	6.48	8.104	9.095	19.128	0.409	0.039	0.030	0.931

Notes.

illustrates how a gas fluid element is processed in this updated version of SÍGAME.

3.1. Dense Phase

SÍGAME uses the method described in Rahmati et al. (2013) to derive the dense gas mass fraction, f_{H_2} , associated with a given fluid element. The dense gas mass is then $m_{\rm dense} =$ $m_{\rm gas}f_{\rm H_2}$, where $m_{\rm gas}$ is the total gas mass of the fluid element. The dense gas is divided into giant molecular clouds (GMCs) by randomly sampling the Galactic GMC mass spectrum over the mass range $10^4 - 10^6 M_{\odot}$ until the remaining dense gas mass is $<10^4 M_{\odot}$, at which point the gas is discarded. If the initial $m_{\rm dense}$ does not exceed this lower limit, no GMCs are associated with the fluid element and $m_{\rm dense}$ is set to zero. No more than 0.01% of the dense gas mass in any of our 30 simulations are discarded during this process. The Galactic GMC mass spectrum adopted here has a power-law slope of 1.8 as derived by Blitz et al. (2007) for the outer MW. In Section 5, we explore the effects of adopting a shallower as well as a steeper spectrum.

Each GMC inherits the metallicity, Z, of its parent fluid element and is subject to an external cloud pressure, $P_{\rm ext}$, which is calculated from the surface densities of stars and star-forming gas as well as their vertical velocity dispersions assuming hydrostatic midplane equilibrium (see Olsen et al. 2015). The

GMC sizes ($R_{\rm GMC}$) are derived from a pressure-normalized mass–size relation (Olsen et al. 2015), which results in cloud radii in the range 5.8 to 43.6 pc (Figure 3). The GMC radial density profiles are assumed to follow a truncated logotropic profile,

$$n_{\rm H}(R) = n_{\rm H,ext} \left(\frac{R_{\rm GMC}}{R}\right),$$
 (1)

where $n_{\rm H}(R > R_{\rm GMC}) = 0$ and the external density, $n_{\rm H,ext}$, is two-thirds of the average density within $R_{\rm GMC}$. The GMCs are randomly distributed within $0.5 \times$ the smoothing length of the fluid element.

Each GMC is assumed to be isotropically irradiated by a local FUV radiation field from nearby young stars and a constant diffuse background FUV field from the overall stellar population of the galaxy. The local field is the cumulative FUV radiation field from stellar particles within one smoothing length of the gas fluid element position (r_{gas}). Each contribution is scaled according to the stellar mass ($m_{*,i}$) and distance ($|r_{gas} - r_{*,i}|$) from the gas element such that the strength of the local field is given by

$$\frac{G_{0,\text{loc}}}{\text{erg cm}^{-2} \,\text{s}^{-1}} = \sum_{|\mathbf{r}_{\text{gas}} - \mathbf{r}_{\text{*},i}| < h} \frac{L_{\text{FUV},i}}{4\pi |\mathbf{r}_{\text{gas}} - \mathbf{r}_{\text{*},i}|^2} \frac{m_{*,i}}{10^4 \, M_{\odot}}, \quad (2)$$

 $^{^{}a}$ $R_{\rm gal}$ is the radius defined by the group finder CAESAR together with the yt project (see text).

^b The SFR was averaged over the past 100 Myr.

 $^{^{}c}$ $\langle Z \rangle_{SFR}$ is the average of the SFR-weighted metallicities, in units of solar metallicity, of the fluid elements belonging to a galaxy.

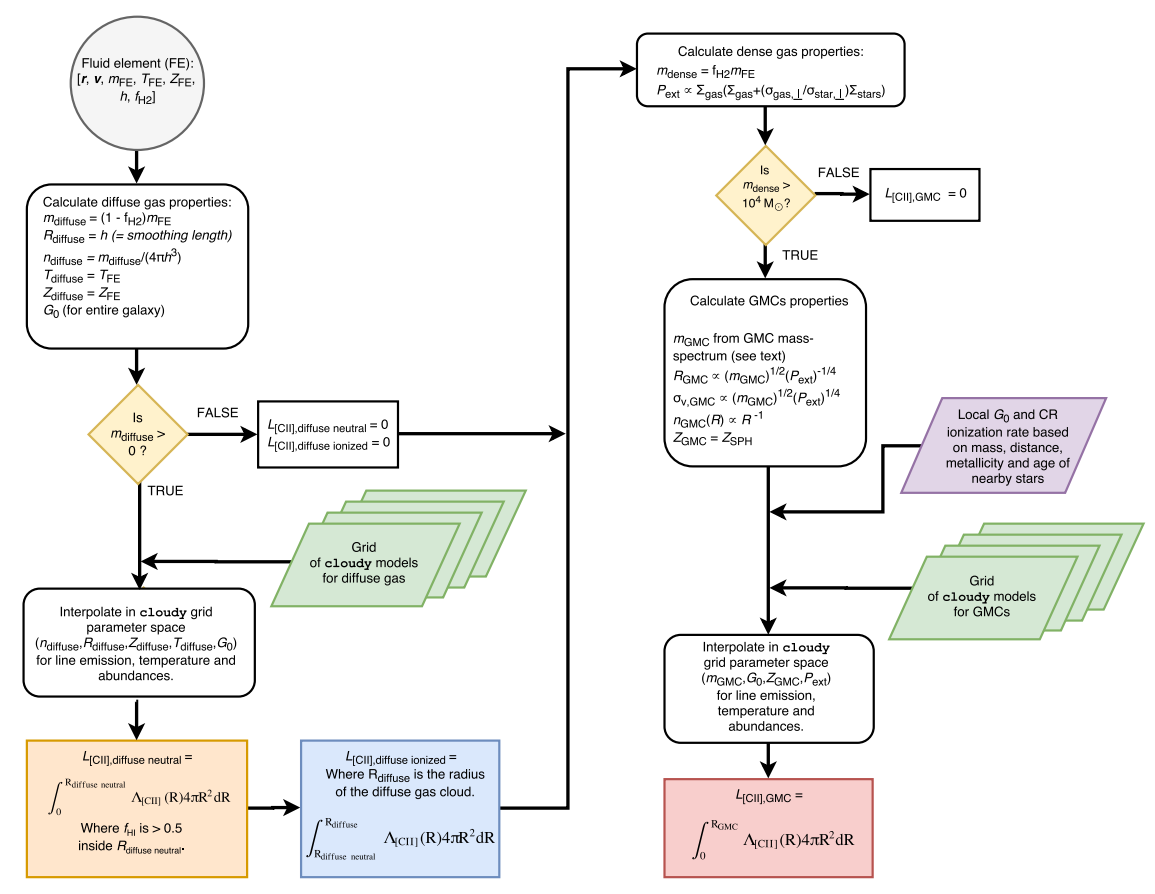


Figure 2. Flowchart of the subgridding procedures applied by SÍGAME to each gas fluid element in the MUFASA simulations.

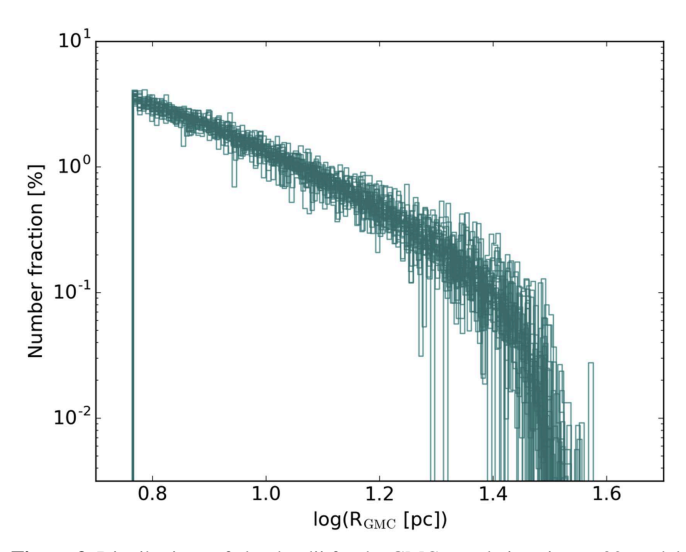


Figure 3. Distributions of cloud radii for the GMC populations in our 30 model galaxies.

where $|r_{\rm gas} - r_{*,i}|$ is in cm and $m_{*,i}$ is in M_{\odot} . $L_{{\rm FUV},i}$ is the FUV luminosity in units of erg s⁻¹ of a $10^4\,M_{\odot}$ stellar population with a metallicity and age the same as those of the *i*th stellar particle. The $L_{{\rm FUV},i}$ values are found by interpolating over a grid of starburst99¹³ (Leitherer et al. 2014) stellar population models of mass $10^4\,M_{\odot}$ and covering the range of metallicities and ages of the stellar populations encountered in

the simulations. These models adopt a Kroupa initial mass function (IMF) and an instantaneous burst star formation history. We note that the hydrodynamic simulations use a slightly different IMF (Chabrier), but expect the differences in UV luminosity to be negligible. The strength of the constant background FUV field is set to

$$\frac{G_{0,\text{bg}}}{\text{erg cm}^{-2} \,\text{s}^{-1}} = G_{0,\text{MW}} \frac{\Sigma_{\text{SFR}}}{\Sigma_{\text{SFR MW}}},\tag{3}$$

where $G_{0,\rm MW}=9.6\times10^{-4}~{\rm erg~cm^{-2}~s^{-1}}$ (=0.6 Habing) is the Galactic FUV field flux (Seon et al. 2011), and $\Sigma_{\rm SFR}$ and $\Sigma_{\rm SFR,MW}$ are the average SFR surface densities of the model galaxy in question and the MW, respectively. $\Sigma_{\rm SFR}$ is defined as the total SFR divided by the area of the galaxy disk seen face-on, using the radii listed in Table 1. Our model galaxies span a range in $\Sigma_{\rm SFR}$ from 0.013 to 0.40 M_{\odot} yr⁻¹ kpc⁻², which corresponds to 4–120 × $\Sigma_{\rm SFR,MW}$ since $\Sigma_{\rm SFR,MW}\simeq0.003~M_{\odot}$ yr⁻¹. The latter is calculated using an SFR of 1.9 M_{\odot} yr⁻¹ (Chomiuk & Povich 2011) and a radius of 13.5 kpc for the star-forming disk of the MW (Kennicutt & Evans 2012).

The total FUV flux impinging on a GMC is $G_{0,\mathrm{GMC}} = G_{0,\mathrm{loc}} + G_{0,\mathrm{bg}}$. For the sake of simplicity, we assume that the spectral shape of this FUV field is identical to that of the standard FUV background in the solar neighborhood (the "ism" table in CLOUDY).

Cosmic rays (CRs) can be an important source of heating and ionization in dense clouds (Papadopoulos et al. 2011, 2014) and

http://www.stsci.edu/science/starburst99/

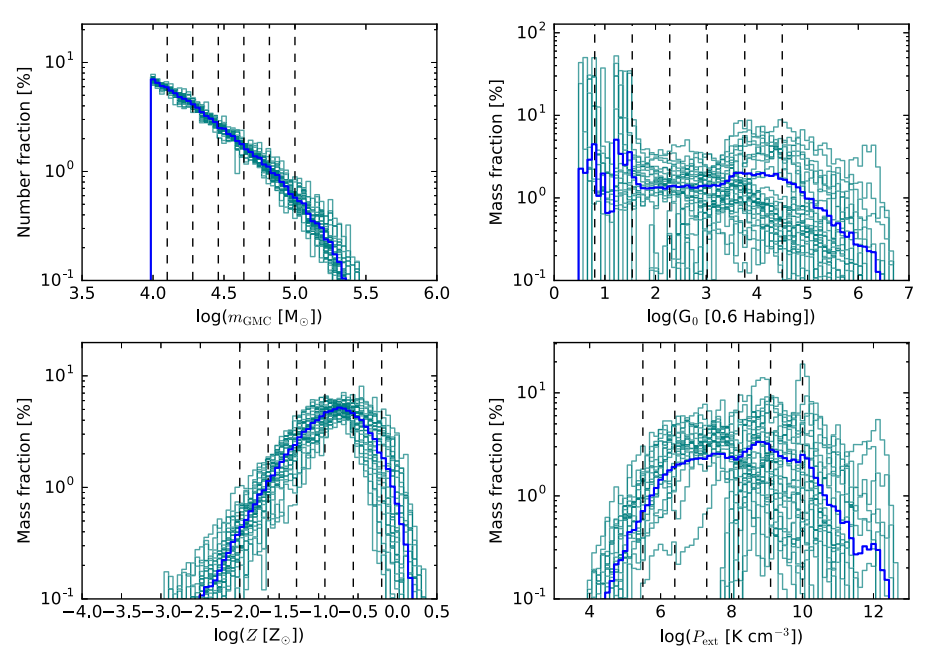


Figure 4. Histograms of m_{GMC} , $G_{0,GMC}$, Z, and P_{ext} of the GMCs in our 30 model galaxies (dark green histograms), with the mean histograms shown in blue. The vertical dashed lines indicate the chosen CLOUDY grid points (see Section 3.3).

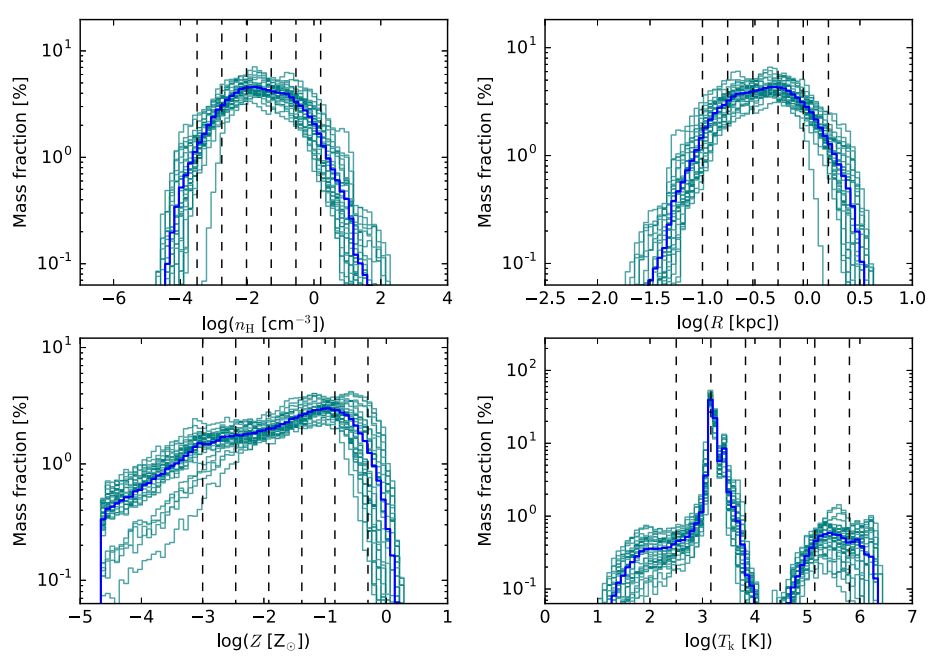


Figure 5. Histograms of n_H , R, Z, and T_k of the diffuse gas clouds in our 30 model galaxies (dark green histograms), with the mean histograms shown in blue. The vertical dashed lines indicate the chosen CLOUDY grid points (see Section 3.3).

are therefore included in the treatment of GMCs in SÍGAME. Each GMC is subjected to a CR ionization rate, which is given by

$$\frac{\zeta_{\text{CR,GMC}}}{\text{s}^{-1}} = \zeta_{\text{CR,MW}} \frac{G_{0,\text{GMC}}}{G_{0,\text{MW}}},\tag{4}$$

where $\zeta_{\rm CR,MW}=3\times 10^{-17}\,\rm s^{-1}$ is the average CR ionization rate in the MW (e.g., Webber 1998).

The distributions of $m_{\rm GMC}$, $G_{0,{\rm GMC}}$, Z, and $P_{\rm ext}$ for the GMC populations in our simulations are shown in Figure 4. Once the GMCs have been configured in the above described manner, CLOUDY is used to calculate the ionization states, thermal

state, and line cooling rates throughout the clouds. The line luminosities of a GMC is calculated as the line cooling rates provided by CLOUDY integrated over the volume of the cloud.

3.2. Diffuse Phase

The diffuse gas mass associated with a fluid element is $m_{\rm diffuse} = m_{\rm gas} - m_{\rm dense}$. Provided $m_{\rm diffuse} > 0$ for the fluid element in question, the diffuse gas is distributed evenly within a spherical region with a radius equal to the smoothing length of the fluid element and centered on its position. Furthermore, the diffuse gas inherits the metallicity and temperature of the fluid element. Figure 5 shows the distributions of densities,

radii, metallicities, and temperatures for the diffuse clouds in our model galaxies.

The clouds of diffuse gas are larger (typical radii are ~ 1 kpc but span the range 0.1-5 kpc) than the dense gas clouds and have lower densities (typical densities are $\sim 10^{-2}$ cm⁻³ but span the range $\sim 10^{-4}-10^2$ cm⁻³). It is assumed that the diffuse clouds are unassociated with star formation sites and, as a result, they are only irradiated (isotropically) by the diffuse background FUV field (i.e., $G_{0,\rm bg}$). The heating and ionization of the diffuse gas is also affected by the presence of CRs, and we set the CR ionization rate felt by the diffuse phase to

$$\frac{\zeta_{\text{CR,bg}}}{\text{s}^{-1}} = \zeta_{\text{CR,MW}} \frac{G_{0,\text{bg}}}{G_{0,\text{MW}}}.$$
 (5)

As was done for the GMCs, CLOUDY is used to calculate the ionization states and line cooling rates throughout the diffuse clouds. SÍGAME uses the output from CLOUDY to define the transition from the inner neutral to the outer ionized regions of the diffuse clouds: the radius where the neutral hydrogen fraction, i.e., the number density of HI divided by the number density of HI and HII, is 0.5. In cases where this fraction is >0.5 at all radii, SÍGAME identifies the entire cloud as diffuse neutral gas. The above procedure allows us to operate with a diffuse neutral and a diffuse ionized gas phase in our simulations, in addition to the dense gas phase. The line luminosities of the neutral and ionized phases within a cloud are calculated by integrating the line cooling rates over the volumes of each of the two phases.

3.3. CLOUDY Model Setup

The main input parameters for CLOUDY in this work are the cloud radius, the radial density profile of the cloud, the FUV spectrum impinging on the cloud, the element abundances, and the gas kinetic temperature. In the following, we describe how each of these parameters are specified for GMCs and diffuse gas clouds.

Cloud radius: for our GMC models, the external pressure is used together with the GMC mass to determine the cloud radius (see Section 3.1), whereas the diffuse clouds have sizes given by the smoothing length of the parent fluid element.

Density profile: the mass and radius are combined to derive the density profile of each GMC (Equation (1)), while the diffuse gas clouds are assigned uniform densities (Section 3.2).

FUV radiation field: the GMCs experience the combination of the local FUV radiation field flux (Equation (2)) and the constant background field (Equation (3)). The diffuse clouds are only exposed to the background field. In both GMCs and diffuse clouds, we adopt a spectral shape and luminosity corresponding to that of the local solar neighborhood, which is then scaled by $G_{0,\mathrm{GMC}}$ and $G_{0,\mathrm{bg}}$, respectively.

Element abundances: in the MUFASA simulations, the abundances of He, C, N, O, Ne, Mg, Si, S, Ca, and Fe (relative to H) are each tracked separately and self-consistently calculated at every time step for each fluid element. While CLOUDY can take an abundance set as the an input parameter, it is infeasible to run CLOUDY models for every distinct abundance pattern present in the MUFASA simulations. Our default approach is to ascribe the local ISM abundances to a cloud (dense or diffuse), but scale all element abundances by the metallicity inherited from the parent fluid element. Specifically, we scale the abundances from CLOUDY such that a sum over the mass fractions of the elements He, C, N, O,

 Table 2

 Adopted Parameter Values for the GMC Grid and Diffuse Gas CLOUDY Grids

Parameter	Grid Point Values				
GMCs					
$\log(m_{\rm GMC}/M_{\odot})$	[4.10, 4.28, 4.46, 4.64, 4.82, 5.00]				
$\log(G_{0,\mathrm{GMC}}/G_{0,\mathrm{MW}})$	[0.80, 1.54, 2.28, 3.02, 3.76, 4.50]				
$\log~(Z/Z_{\odot})$	[-2.00, -1.64, -1.28, -0.92, -0.56, -0.20]				
$\log (P_{\rm ext}/{\rm K~cm}^{-3})$	[5.5, 6.4, 7.3, 8.2, 9.1, 10.0]				
Diffuse Gas					
$\log (n_{\rm H}/{\rm cm}^{-3})$	[-3.50, -2.76, -2.02, -1.28, -0.54, 0.20]				
log (R/kpc)	[-1.00, -0.76, -0.52, -0.28, -0.04, 0.20]				
$\log (Z/Z_{\odot})$	[-3.00, -2.46, -1.92, -1.38, -0.84, -0.30]				
$\log(T_{\rm k}/{\rm K})$	[2.50, 3.16, 3.82, 4.48, 5.14, 5.80]				
$G_{0, m bg}/G_{0, m MW}$	[5, 35]				

Ne, Mg, Si, S, Ca, and Fe for a fluid element with solar metallicity gives 0.0134 as expected (Asplund et al. 2009).

Gas kinetic temperature: in the GMCs, CLOUDY is allowed to iterate for a temperature. For the diffuse clouds, we keep the temperature fixed at the grid parameter values listed in Table 2.

The dust content of each cloud is set to scale linearly with its metallicity, normalizing it to the grain abundance in the local ISM. The latter is stored in CLOUDY as graphite and silicate grain abundances divided into 10 size bins, and corresponds to a dust-to-metal (DTM) ratio of 0.50 at solar metallicity. Furthermore, dust sublimation is included in the diffuse gas models to allow for dust destruction in regions of high temperature. CLOUDY also allows for the inclusion of turbulence by specifying a microturbulent velocity. For the diffuse clouds, we exclude turbulence by setting it to 0 km s⁻¹, after a test showed that setting the turbulence to 10 km s⁻¹ only decreases the [C II] luminosities by 0.07 dex on average. For the GMCs, we use the velocity dispersion obtainable from the cloud radius and pressure (see Olsen et al. 2015).

At $z\sim6$, the CMB temperature is substantial ($\sim19~\rm K$) and is included in the calculations of CLOUDY with the "CMB command." The line intensities are corrected to give the net line flux above the background continuum, including the diminution effect that happens when the upper population levels are sustained by the CMB and reduce the rate of spontaneous deexcitations relative to when excitation happens by collisions only (see Ferland et al. 2017 for a more complete description of the CMB treatment in CLOUDY version 17).

CLOUDY divides each cloud into a number of shells when solving the radiative transfer, heat transfer, and chemistry. We set the number of shells to \sim 50, leading to a radial resolution in the range $\sim 0.01-0.52$ pc for the GMCs and $\sim 1-100$ pc for the diffuse gas clouds. Due to computational limitations that make it infeasible to run CLOUDY on every single cloud in our simulations, we construct grids of CLOUDY models, one grid for GMCs and another for the diffuse clouds, and interpolate over those. The GMC grid parameters consist of $[m_{GMC}, G_{0,GMC}]$ Z, P_{ext}] and the diffuse cloud parameters are $[n_{\text{H}}, R, Z, T_{\text{k}}]$. We ran diffuse gas model grids with $G_{0,\rm bg}/G_{0,\rm MW}=5$ and 35 (Equation (3)), which were the two values most of the galaxies clustered around. One galaxy (G21) has a diffuse FUV field of $120 \times G_{0,MW}$, but adding a further four diffuse gas model grids at $G_0/G_{0,MW} = 15$, 25, 45, and 120 to better sample the distribution did not significantly change the line emission properties of the simulations. The grid parameter values defining our grids are listed in Table 2, and indicated as vertical dashed

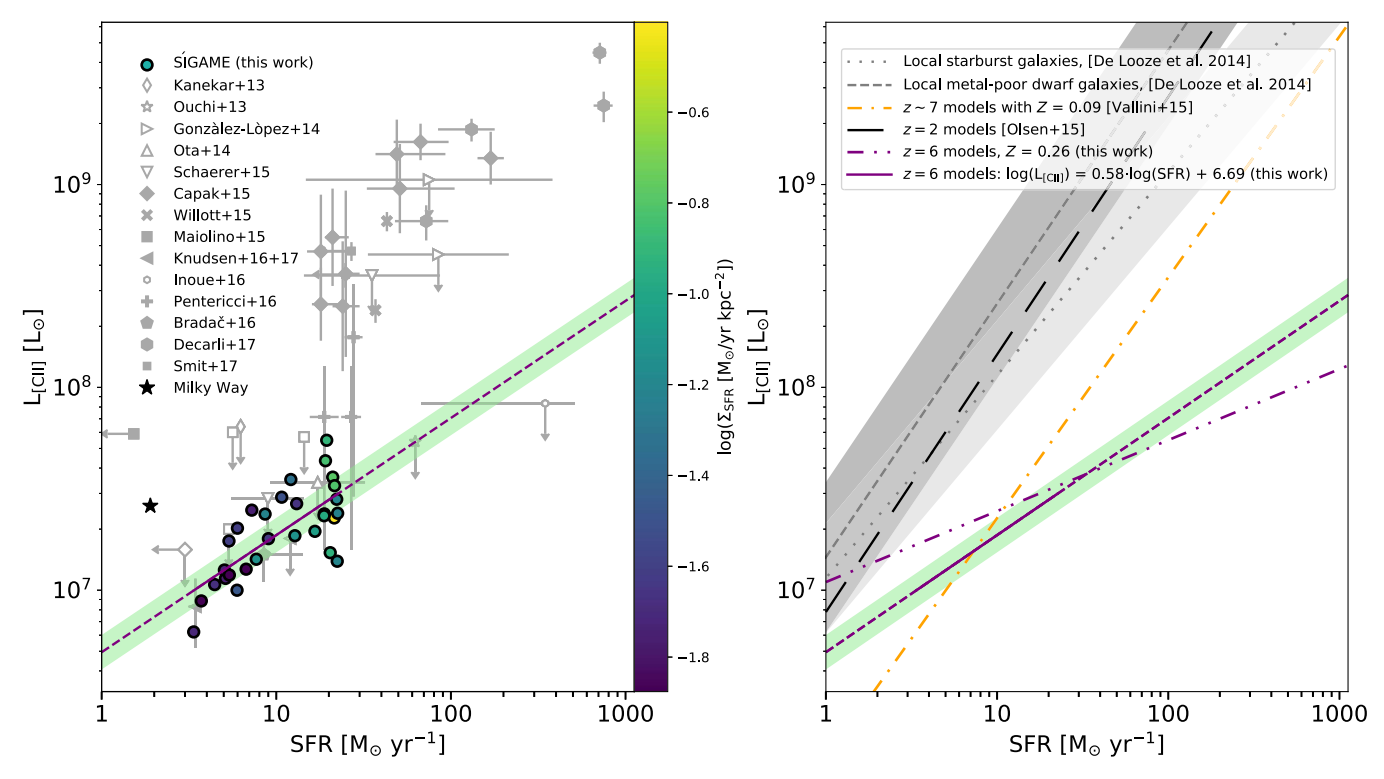


Figure 6. Left: [C II] luminosity vs. SFR for our simulations, and the green shaded region delineates the scatter (0.13 dex) around this relation. For comparison, all [C II] observations to date of LBGs and/or LAEs at $z \gtrsim 5$ are shown (gray symbols, where filled and open symbols indicate detections and 3σ upper limits, respectively). For further details on the observations, see Kanekar et al. (2013), Ouchi et al. (2013), González-López et al. (2014), Ota et al. (2014), Schaerer et al. (2015), Capak et al. (2015), Willott et al. (2015), Maiolino et al. (2015), Inoue et al. (2016), Pentericci et al. (2016), Knudsen et al. (2016, 2017), Bradač et al. (2017), Decarli et al. (2017), and Smit et al. (2017). For the sake of clarity, we have not included MS0451-H (z = 6.703) in the plot. This source has $L_{[C II]} < 3 \times 10^5 L_{☉}$ and SFR $\sim 0.4 \, M_{☉} \, \text{yr}^{-1}$ (Knudsen et al. 2017), and lies about 1 dex below our fitted relation. All SFRs have been converted to a Chabrier IMF where applicable. Right: a comparison with other, observed and simulated, [C II]–SFR relations. Shown are the [C II]–SFR relations derived by De Looze et al. (2014) for local metal-poor dwarf galaxies (gray dashed line) and local starburst galaxies (gray dashed line) indicating the rms scatter of these relations. Also shown are simulated relations of the z = 2 main sequence galaxies (black long-dashed line; Olsen et al. 2015) and $z \sim 7$ galaxies (orange dashed–dotted line; Vallini et al. 2015).

lines in Figures 4 and 5. Each grid consists of a total of 1296 CLOUDY models. The CLOUDY models were run on either the Stampede supercomputer at the Texas Advanced Computing Center, ¹⁴ the Saguaro cluster at ASU, ¹⁵ or the Pleiades supercomputer at NASA. ¹⁶

4. Simulation Results

4.1. The
$$L_{[CII]}$$
-SFR Relation at $z \simeq 6$

Figure 6 (left panel) shows $L_{\rm [C\ II]}$ against SFR for our model galaxies (filled circles). There seems to be a correlation between these two quantities, although our simulations only span about a decade in [C II] luminosity and SFR, and there is significant scatter in $L_{\rm [C\ II]}$, especially at the high-SFR end. A Pearson correlation coefficient test yields an R-value of 0.64 and a p-value of 0.00014 for the likelihood that the observed correlation could arise by chance if the quantities were uncorrelated. We can therefore meaningfully fit a log-linear relationship to the simulation points in Figure 6. This yields

$$\log(L_{\rm [C II]}[L_{\odot}]) = (6.69 \pm 0.10) + (0.58 \pm 0.11) \times \log({\rm SFR}[M_{\odot} \, {\rm yr}^{-1}]),$$
 (6)

which is shown as the purple dashed line in Figure 6. The uncertainties on the slope and intercept were derived from bootstrapping the model results 5000 times. The rms scatter of the simulated galaxies around this relation is 0.15 dex (green shaded region).

Also shown in Figure 6 are the more than two dozen $z\gtrsim 5$ galaxies observed in [C II] to date: 23 detections (filled symbols) and 14 non-detections (upper limits, open symbols). Only normal star-forming galaxies (e.g., LBGs and LAEs) were included in this tally (see Table 3)—possibly with the exception of a clump of gas that may not be star forming but was detected in [C II] in the vicinity of LBG BDF-3299 (Maiolino et al. 2015). Obvious AGN-dominated sources and quasi-stellar objects (QSOs) have been omitted.

Based on these data, it would seem there is not a single $L_{\rm [CIII]}$ – SFR relation. There is a relation defined mainly by the $z\sim5$ –6 LBGs with SFR $\gtrsim20\,M_\odot$ yr $^{-1}$ observed by Capak et al. (2015), Willott et al. (2015), Decarli et al. (2017), and Smit et al. (2017), which matches the locally observed $L_{\rm [C\,II]}$ –SFR relation for starburst galaxies (De Looze et al. 2014) and is in agreement with simulations of main-sequence galaxies at $z\sim2$ (Olsen et al. 2015; see the right-hand panel of Figure 6). Offset from these points, there is a sequence of galaxies with significantly lower [C II] luminosities. These are predominantly LAEs with SFR < 30 M_\odot yr $^{-1}$, except for two notable high-SFR sources (Ouchi et al. 2013; Inoue et al. 2016). Since the majority of these sources have in fact only

https://www.tacc.utexas.edu/systems/stampede

¹⁵ https://researchcomputing.asu.edu/

¹⁶ https://www.nas.nasa.gov/hecc/resources/pleiades.html

Table 3
All [C II] Observations in the Literature of $z \gtrsim 5$ Star-forming Galaxies to Date

Name	z	$SFR^a (M_{\odot} yr^{-1})$	$L_{ m [C~II]}(L_{\odot})$	μ^{b}	References
HZ8	5.1533	18 ^c	2.57×10^{9}	•••	Capak et al. (2015)
HZ7	5.2532	21 ^c	5.50×10^9	•••	Capak et al. (2015)
HZ6	5.2928	49 ^c	1.41×10^{10}		Capak et al. (2015)
HZ5	5.3089	<3°	$< 1.58 \times 10^{7}$		Capak et al. (2015)
HZ9	5.5410	67 ^c	1.62×10^{10}	•••	Capak et al. (2015)
HZ3	5.5416	18 ^c	4.68×10^{8}		Capak et al. (2015)
HZ4	5.5440	51 ^c	9.55×10^{8}		Capak et al. (2015)
HZ10	5.6566	169 ^c	1.34×10^{10}	•••	Capak et al. (2015)
HZ2	5.6697	25 ^e	3.63×10^{8}	•••	Capak et al. (2015)
HZ1	5.6885	24 ^c	2.51×10^{8}	•••	Capak et al. (2015)
A383-5.1	6.0274	$3.2-3.7^{d}$	$< 8.3 \times 10^6$	11.4 ± 1.9	Knudsen et al. (2016)
SDSS J0842+1218 comp	6.0656	131 ^e	1.87×10^{9}		Decarli et al. (2017)
WMH5	6.0695	43 ^f	6.6×10^{8}	1.27	Willott et al. (2015)
CFHQ J2100-1715 comp	6.0796	750 ^e	2.45×10^{9}	•••	Decarli et al. (2017)
CLM1	6.1657	37^{f}	2.4×10^{8}	•••	Willott et al. (2015)
PSO J308-21 comp	6.2485	72 ^e	6.6×10^{8}		Decarli et al. (2017)
SDF J132415.7	6.541	34–211.2 ^d	$< 4.52 \times 10^{8}$	<1.1	González-López et al. (2014)
SDF J132408.3	6.554	15-375.9 ^d	$< 10.56 \times 10^{8}$	<1.1	González-López et al. (2014)
HCM 6A	6.56	6.25^{f}	$< 0.64 \times 10^8$	≈4.5	Kanekar et al. (2013)
PSO J231-20 comp	6.5900	713 ^e	4.47×10^9	•••	Decarli et al. (2017)
Himiko	6.595	62.5 ^f	$< 0.54 \times 10^8$		Ouchi et al. (2013)
UDS16291	6.6381	15.8–22.4 ^d	7.15×10^{7}	•••	Pentericci et al. (2016)
NTTDF6345	6.701	25–30.7 ^d	1.77×10^{8}		Pentericci et al. (2016)
MS0451-H	6.703	$0.4-0.47^{d}$	$< 3 \times 10^{5}$	100 ± 20	Knudsen et al. (2016)
RXJ1347:1216	6.7655	8.5 ^f	1.5×10^{7}	5 ± 0.3	Bradač et al. (2017)
A1703-zD1	6.8	5.6–14.3 ^d	$< 2.83 \times 10^{7}$	~ 9	Schaerer et al. (2015)
COS-2987030247	6.8076	16–38.7 ^d	3.6×10^{8}	•••	Smit et al. (2017)
SDF-46975	6.844	14.4 ^c	$< 5.7 \times 10^7$	•••	Maiolino et al. (2015)
COS-3018555981	6.8540	19–38.2 ^d	4.7×10^{8}	•••	Smit et al. (2017)
IOK-1	6.96	9.4–31.8 ^d	$< 3.4 \times 10^{7}$	•••	Ota et al. (2014)
BDF-512	7.008	5.6°	$< 6 \times 10^{7}$	•••	Maiolino et al. (2015)
BDF-3299 (clump A)	7.107	<1.5°	5.9×10^{7}	•••	Maiolino et al. (2015)
BDF-3299	7.109	5.3°	$< 2 \times 10^{7}$	•••	Maiolino et al. (2015)
COSMOS13679	7.1453	23.9–30 ^d	7.12×10^{7}	•••	Pentericci et al. (2016)
SXDF-NB1006-2	7.2120	347 ^f	$< 8.4 \times 10^{7}$	•••	Inoue et al. (2016)
z8-GND-5296	7.508	14.6–85.3 ^d	$< 3.56 \times 10^{8}$	~9	Schaerer et al. (2015)
A1689-zD1	7.6031	12 ^f	1.8×10^{7}	9.5	Knudsen et al. (2017)

Notes. Obvious AGN-dominated sources and QSOs are not included. Star formation rates and [C II] luminosities were corrected for gravitational magnification (μ). Upper limits are 3σ limits.

(This table is available in machine-readable form.)

upper limit constraints on their [C II] luminosity (Kanekar et al. 2013; Ota et al. 2014; Maiolino et al. 2015; Knudsen et al. 2017), it is not clear whether or not they form an $L_{\rm [C II]}$ -SFR relation of their own. However, the fact that our simulated galaxies coincide with these [C II]-faint sources in the panel suggests that our models are representative of the observations. Furthermore, Equation (6) is consistent with the two high-SFR, [C II] upper limits by Ouchi et al. (2013) and Inoue et al. (2016). On the other hand, MS0451-H (z=6.703; Knudsen et al. 2017) with its extremely low [C II] luminosity ($<3 \times 10^5 L_{\odot}$) and SFR ($\sim 0.4 \, M_{\odot} \, \text{yr}^{-1}$) falls below Equation (6) by about 1 dex (not shown due to the axis range of the Figure 6). Clearly, more sensitive observations, and of a

larger sample of galaxies, are required to delineate a [C II]-SFR relation at this epoch.

In Figure 6 (right panel), we compare our Equation (6) with the $z\simeq 7$ [C II]—SFR relation by Vallini et al. (2015). The latter is derived from a fiducial simulation of a single $z\sim 7$ galaxy, and scaling its $L_{\rm [C~II]}$ and SFR according to $L_{\rm [C~II]}\propto M_{\rm H_2}$ and $\Sigma_{\rm SFR}\propto \Sigma_{\rm H_2}$. Also, the gas phase metallicity of the galaxy is fixed to a constant value throughout the galaxy and therefore bears no relation to its star formation history. By adopting a set of fixed metallicities, Vallini et al. (2015) arrive at an expression for $L_{\rm [C~II]}$ as a function of SFR and metallicity. The orange dashed—dotted line in the right-hand side panel shows their [C II]—SFR relation for a uniform metallicity equal

^a SFRs are for a Chabrier IMF. SFRs based on either a Kroupa or Salpeter IMF were corrected by a factor of 1.5/1.6 and 1/1.6, respectively.

^b Where the magnification factor is unknown, we assume a value of 1.

c UV-based SFR.

^d Low SFRs are derived from the UV; high SFRs are from the UV combined with an upper limit in the IR.

e IR-based SFR.

f SED-based SFR.

to the mean mass-weighted metallicity of our simulated galaxies $(0.09 \times Z_{\odot})$. This relation matches our simulated galaxies surprisingly well given the significant differences between their simulations and ours (see Section 5). Clearly, at SFR values outside the range of our simulations, there is significant discrepancy between the [C II]–SFR relation by Vallini et al. (2015) and ours (Equation (6)), owing to the much shallower slope of the latter (0.58 \pm 0.11 versus 1.2). Extrapolating Equation (4) to SFRs well outside the range of the simulations is obviously fraught with danger, and any comparison must be made with caution. This is especially true given that Equation (4) is a fit to a set of simulations that spans no more than a decade in SFR and $L_{\rm [C\ II]}$.

4.2. ISM Phases and [C II]

The mass fractions of each ISM phase stay relatively constant across the 30 simulated galaxies: the GMCs, and the diffuse neutral and diffuse ionized gas take up on average $\sim 10\%$, $\sim 6\%$, and $\sim 85\%$ of the total ISM mass, respectively, and there is no apparent trend with SFR or $\langle Z \rangle_{\rm mass}$ (Figure 7, top panels). In contrast, the contribution of these ISM phases to the total [C II] luminosity can vary significantly from one simulated galaxy to another. The GMCs take up $\sim 5\%-63\%$ (average $\sim 27\%$), the diffuse neutral gas $\sim 1\%-23\%$ (average $\sim 7\%$), and the diffuse ionized gas $\sim 3\%-90\%$ (average $\sim 66\%$) of the total [C II] luminosity. The dominant source of [C II] in the simulated galaxies is either the diffuse ionized gas or the GMCs, with the diffuse neutral gas making up a minor contribution ($\lesssim 23\%$).

In Figure 7 (middle panels), the ISM phase contributions to $L_{\rm [C\,II]}$ are shown as a function of galaxy SFR (left panel) and $\langle Z \rangle_{\rm mass}$ (right panel). The contribution from the diffuse ionized gas, which is the dominant phase in nearly all of the galaxies, tends to increase slightly toward the high end of the SFR and $\langle Z \rangle_{\rm mass}$ distributions. For the GMCs and the diffuse neutral gas, the tendency is in the opposite direction, i.e., their contributions tend to increase toward lower SFR and $\langle Z \rangle_{\rm mass}$.

In the Vallini et al. (2015) models with SFRs similar to our simulations, $\lesssim 10\%$ of the total [C II] emission is coming from diffuse neutral gas, with the remainder coming from PDRs associated with molecular gas. Thus, to the extent that the diffuse neutral gas in the two simulations map onto each other, there is broad agreement about the contribution of this phase to the total [C II] luminosity. The lower [C II] contributions from molecular gas in our simulations compared to the Vallini et al. (2015) models (\sim 37% versus \gtrsim 90%) must, in part at least, be due to the fact that Vallini et al. (2015) do not include a hot diffuse ionized phase. In contrast, the diffuse ionized gas mass fraction in our simulations is \sim 85% on average and is responsible for more than half of the total [C II] luminosity in most of our simulations. In our Milky Way, dense PDRs and CO-dark H2 gas is responsible for about \sim 55% of the total [C II] emission, while the diffuse ionized gas and diffuse neutral gas contribute $\sim 20\%$ and 25%, respectively (Pineda et al. 2014). Cormier et al. (2012) used CLOUDY to model the ISM of the nearby ($z \sim 0.021$) starburst galaxy Haro 11, which has a metallicity ($\sim 0.3 Z_{\odot}$) and SFR (\sim 22 M $_{\odot}$ yr $^{-1}$) matching those of our simulations, and found that 10% of the [C II] luminosity comes from dense PDRs and about 50% from the diffuse ionized medium.

We saw that the galaxy-to-galaxy variations in the relative $[C \ II]$ contributions from the ISM phases are not matched by their (nearly constant) mass fractions. This suggests that the

ability of a given ISM phase to shine in [C II] can change significantly among different galaxies. In order to investigate this, we plot in Figure 7 (bottom panels) the [C II] efficiency, defined as [C II] luminosity over gas mass, in order of increasing SFR (left panel) and $\langle Z \rangle_{mass}$ (right panel).

Although there are notable exceptions, the [C II] efficiencies of all three phases tend to increase with SFR and with $\langle Z \rangle_{\rm mass}$. The trend with metallicity is easily understood, as an increase in the carbon abundance will result in a higher abundance of C⁺. The trend with SFR is a combination of the fact that our simulations with higher SFRs have higher metallicities (see Table 1) and the fact that, on average, they have stronger FUV radiation fields capable of ionizing a larger fraction of the neutral carbon in the GMC and diffuse neutral phase.

4.3. [O I] and [O III] at
$$z \simeq 6$$

In this section, we will examine the [O I] 63 μ m and [O III] 88 μ m line emission from our simulations. Figure 8 shows the [OI] and [OIII] luminosities versus SFRs for our simulated galaxies, along with local $L_{\mathrm{[O\ II]}}-\mathrm{SFR}$ and $L_{\mathrm{[O\ III]}}-\mathrm{SFR}$ relations established for samples of local metal-poor dwarfs and starburst galaxies (De Looze et al. 2014). Both the [O I] and [O III] simulations overlap with the local relations, although the agreement is significantly better for [O III] than for [O I]. In fact, the [OI] simulations exhibit no correlation with SFR: a Pearson correlation test of $log(L_{O I})$ versus log(SFR) gives R and p-values of -0.08 and 0.69, respectively. In contrast, [O III] shows a strong correlation with SFR, and a Pearson correlation test of $log(L_{O III})$ versus log(SFR) yields R=0.79and $p = 2.5 \times 10^{-7}$, respectively. Thus, the [O III] luminosities of our simulations correlate more strongly with SFR than [C II]. A log-linear fit yields

$$\log(L_{\rm [O\,III]}[L_{\odot}]) = (6.27 \pm 0.14) + (1.12 \pm 0.17) \times \log(SFR[M_{\odot} \, yr^{-1}]),$$
 (7)

which is shown as the purple dashed line in Figure 8. The uncertainties on the slope and intercept were inferred from bootstrapping in a similar way as for [C II] (Section 4.1). The [O III] detection by Laporte et al. (2017) of a z = 8.38 starforming galaxy (SFR $\simeq 20 \ M_{\odot} \ yr^{-1}$) matches extremely well our simulations with similar SFRs. Furthermore, extrapolating Equation (7) to the SFR ($\sim 250 \,\mathrm{M}_{\odot} \,\mathrm{yr}^{-1}$) of the detected LAE at z = 7.21 (Inoue et al. 2016) also results in an excellent match. Carniani et al. (2017) also reported three "blind" [O III] detections in the vicinity of BDF-3299 (and at the same redshift). In Figure 8, we only show the [O III] detection spatially closest to the clump detected in [C II] emission (Maiolino et al. 2015). Based on a comparison between models and this [O III] detection, Carniani et al. (2017) find that an in situ SFR of $\sim 7\,M_{\odot}\,{\rm yr}^{-1}$ is required ($\sim 6.6\,M_{\odot}\,{\rm yr}^{-1}$ when converted from a Kroupa to a Chabrier IMF), bringing this object into agreement with the local metal-poor galaxies, but still about 1 dex above our models. The [O III] luminosities of the remaining two sources are 2.2 and $5.8 \times 10^8 L_{\odot}$ (Carniani et al. 2017).

4.4. [C II] Luminosity and Global Galaxy Properties

In addition to the SFR, there are likely a number of other galaxy properties affecting the [C II] emission. For example, in

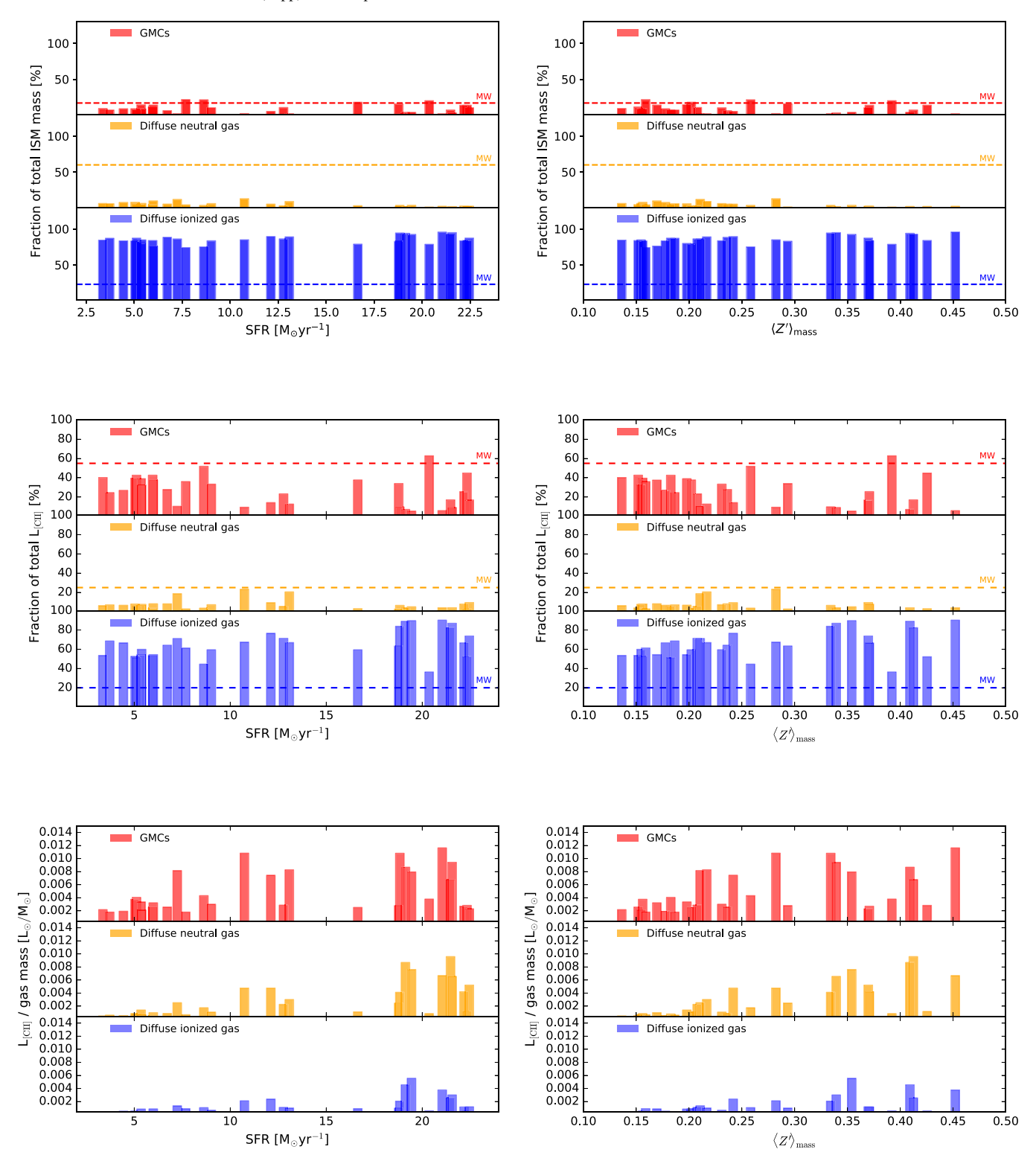


Figure 7. Top: mass fractions of the three ISM phases of our simulated galaxies as a function of their total SFRs (left panel) and mass-weighted average metallicities, $\langle Z \rangle_{mass}$ (right panel). The three ISM phases, GMCs, diffuse neutral gas, and diffuse ionized gas, are shown as red, orange, and blue shaded regions, respectively. The corresponding mass fractions in the MW are shown with horizontal dashed lines: 17% H₂ (red), 60% H I (orange), and 23% H II (blue) within 20 kpc with numbers from Draine (2011). Middle: the contributions from the ISM phases to the total [C II] luminosities vs. SFRs (left panel) and $\langle Z \rangle_{mass}$ (right panel). The horizontal dashed lines indicate the corresponding fractions for the MW (Pineda et al. 2014). Bottom: the [C II] luminosity per gas mass of each ISM phase vs. SFRs (left panel) and $\langle Z \rangle_{mass}$ (right panel).

Section 4.2, we found that the relative ISM phase contributions to the total [C II] luminosity of our simulated galaxies varied not only with SFR but also with the average mass-weighted metallicity of the galaxies. This would suggest that the

metallicity might have an effect on the $L_{\rm [C II]}$ –SFR relation. The simulations by Vallini et al. (2015) exhibited an increase in the [C II] emission with metallicity, which at a basic level is expected since the [C II] cooling function scales linearly with

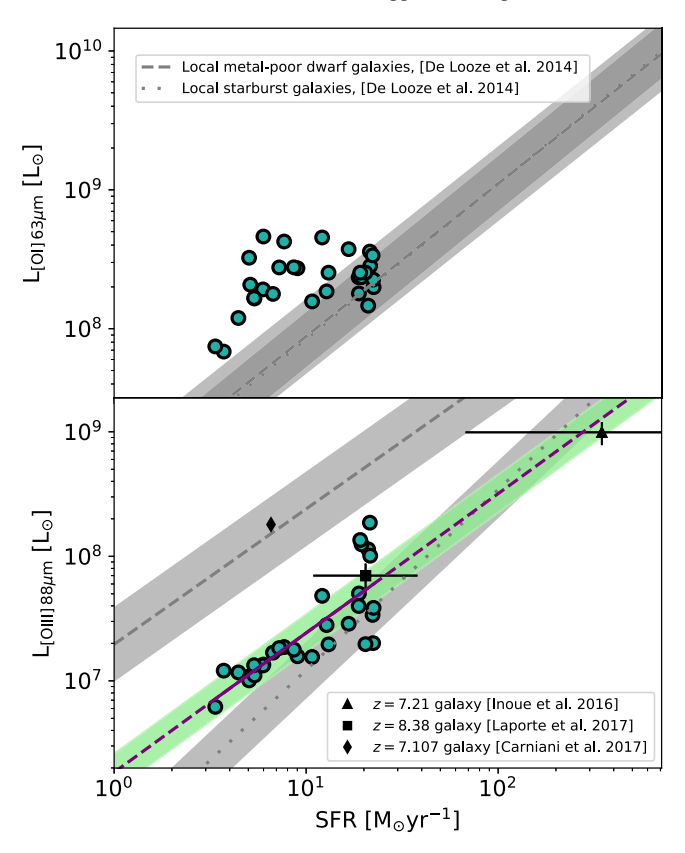


Figure 8. $L_{[O\,II]}$ vs. SFR (top) and $L_{[O\,III]}$ vs. SFR (bottom) for our simulated galaxies (filled circles) compared to the $z\gtrsim 5$ observations of the two lines. A log-linear fit to the $[O\,III]$ simulations is shown by the purple dashed line with a 1σ scatter (0.15 dex) in $L_{[O\,III]}$ as indicated by the green shaded region. Local relations for metal-poor dwarf galaxies (gray dashed lines) and local starburst galaxies (gray dotted lines) are shown for comparison (De Looze et al. 2014). The gray shaded regions indicate the $\pm 1\sigma$ scatter around these relations. Also shown are the detections to date of $[O\,III]$ in star-forming galaxies at $z\gtrsim 5$ (Inoue et al. 2016; Carniani et al. 2017; Laporte et al. 2017).

the gas phase metallicity (Röllig et al. 2006). Observations of nearby galaxies have also found that the surface density of SFRs, Σ_{SFR} , can be important for the total amount of [C II] emitted. For example, Smith et al. (2017) found that the ratio of [C II]-to-IR luminosity decreases with increasing Σ_{SFR} across six orders of magnitude in Σ_{SFR} . Finally, we might expect that the more massive the gas reservoir of a galaxy, the more single ionized carbon is available and, therefore, the brighter the galaxy will shine in [C II].

In Figure 9, we plotted the $L_{\rm [C\ II]}$ of our simulated galaxies against their $\langle Z \rangle_{\rm SFR}$, $\Sigma_{\rm SFR}$, and $M_{\rm ISM}$ (these quantities are given in Table 1, and $M_{\rm ISM} = M_{\rm gas}$). $L_{\rm [C\ II]}$ appears to correlate with $\langle Z \rangle_{\rm SFR}$ and $\Sigma_{\rm SFR}$, whereas there seems to be no discernible correlation with $M_{\rm ISM}$ —perhaps due to the small range spanned in gas mass by our simulations.

In order to better examine the dependence of $L_{\rm [C\ II]}$ on the above quantities and to account for their interdependence, we perform a principal component analysis (PCA; Jolliffe 2002). Normalizing the logarithm of the aforementioned quantities (and SFR) to zero mean leaves the following variables for the PCA:

$$x_1 = \log(\text{SFR}) - 1.02$$

 $x_2 = \log(\langle Z \rangle_{\text{SFR}}) - (-0.61)$
 $x_3 = \log(\Sigma_{\text{SFR}}) - (-1.33)$
 $x_4 = \log(M_{\text{ISM}}) - 10.04.$ (8)

The resulting principal components in this four-dimensional parameter space are

$$PC_{1} = 0.52x_{1} + 0.28x_{2} + 0.80x_{3} - 0.10x_{4}$$

$$PC_{2} = 0.64x_{1} + 0.36x_{2} - 0.48x_{3} + 0.47x_{4}$$

$$PC_{3} = 0.53x_{1} - 0.45x_{2} - 0.27x_{3} - 0.66x_{4}$$

$$PC_{4} = 0.18x_{1} - 0.76x_{2} + 0.22x_{3} + 0.57x_{4}.$$
(9)

Eighty-eight percent of the sample variance is contained within the eigenvector PC_1 , which is dominated by and increases strongly with SFR and Σ_{SFR} . PC_2 , PC_3 , and PC_4 contain $\sim 9\%$, 0.6%, and 2.3% of the variance, respectively. Thus, of the global galaxy properties considered, the star formation activity is the most important factor for driving the [C II] luminosity.

Keeping all four principal components, a regression can be made to

$$\log(L_{[C II]}) = \beta_0 + \beta_1 PC_1 + \beta_2 PC_2 + \beta_3 PC_3 + \beta_4 PC_4,$$
(10)

leading to the following relation for $L_{[C II]}$,

$$\begin{split} \log(L_{\rm [C\ II]}) &= 7.17 - 0.45 \log({\rm SFR}) + 0.89 \log(\langle Z \rangle_{\rm SFR}) \\ &+ 0.66 \log(\Sigma_{\rm SFR}) + 1.88 \log(M_{\rm ISM}). \end{split} \tag{11}$$

In Figure 10 (right-hand panel), we show the [C II] luminosities obtained by applying Equation (11) to our model galaxies plotted against their true [C II] luminosities from the simulations. The scatter between the true [C II] luminosities of the galaxies and Equation (11) is only 0.18 dex, suggesting that Equation (11) captures most of the [C II] dependencies on global galaxy parameters. Repeating the above PCA and regression analysis but using only (SFR, $\langle Z \rangle_{\rm SFR}$, $\Sigma_{\rm SFR}$) and (SFR, $\langle Z \rangle_{\rm SFR}$) as free parameter sets, we obtain

$$\begin{split} \log(L_{\rm [C \, II]}) &= 7.17 \, - \, 0.58 \log({\rm SFR}) \, + \, 0.23 \log(\langle Z \rangle_{\rm SFR}) \\ &- \, 0.02 \log(\Sigma_{\rm SFR}), \end{split} \label{eq:logL}$$
 (12)

and

$$\log(L_{\rm [C II]}) = 7.17 + 0.55 \log({\rm SFR}) + 0.23 \log(\langle Z \rangle_{\rm SFR}), \tag{13}$$

respectively. It is seen that limiting the free parameters to (SFR, $\langle Z \rangle_{\rm SFR}$, $\Sigma_{\rm SFR}$) (middle panel) or (SFR, $\langle Z \rangle_{\rm SFR}$) (left panel) deteriorates the correlations somewhat, with a slight increase in the scatter as a result (0.21 dex).

5. Discussion

5.1. Simulation Robustness

In this section, we examine the effects on the simulation outcomes when changing some of the assumptions build into SÍGAME (Section 3). To this end, we ran SÍGAME on the same 30 MUFASA simulations presented in Section 2 but with changes made to (1) the dust-to-metals (DTM) mass ratio, (2) the slope of the GMC mass spectrum, or (3) the element abundances.

The dust-to-metals mass ratio. The simulations presented in this paper adopted a DTM mass ratio of 0.5, close to the \sim 0.62 of the MW (the latter derived from an average over 243 lines of sight through the local part of our Galaxy; Wiseman et al.

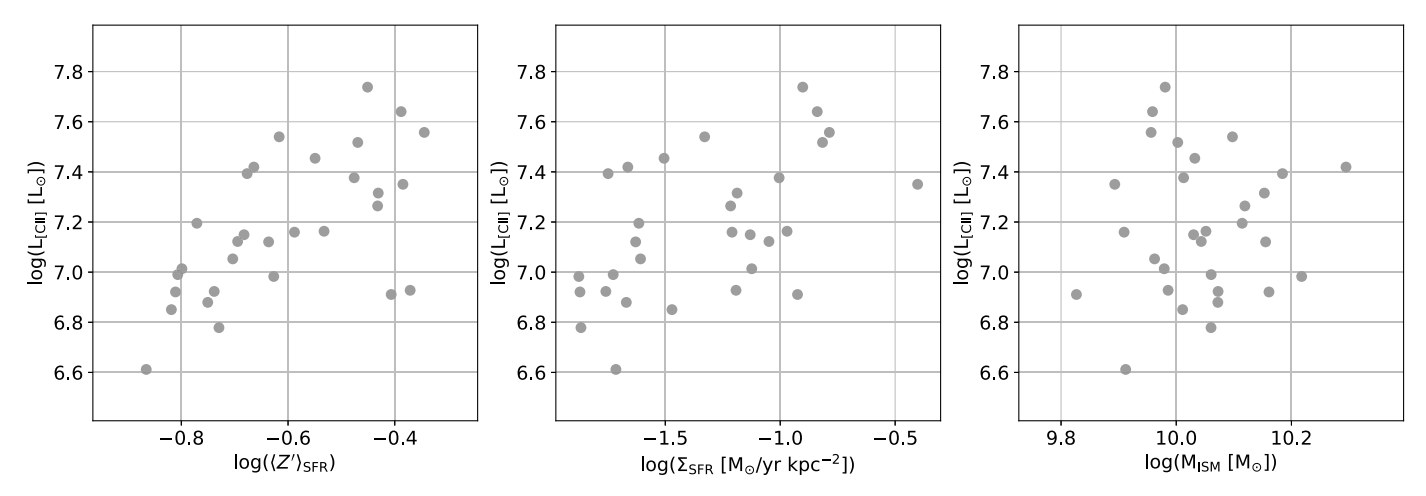


Figure 9. $L_{[C II]}$ vs. $\langle Z \rangle_{SFR}$ (left), Σ_{SFR} (middle), and M_{ISM} (right) for the simulated galaxies.

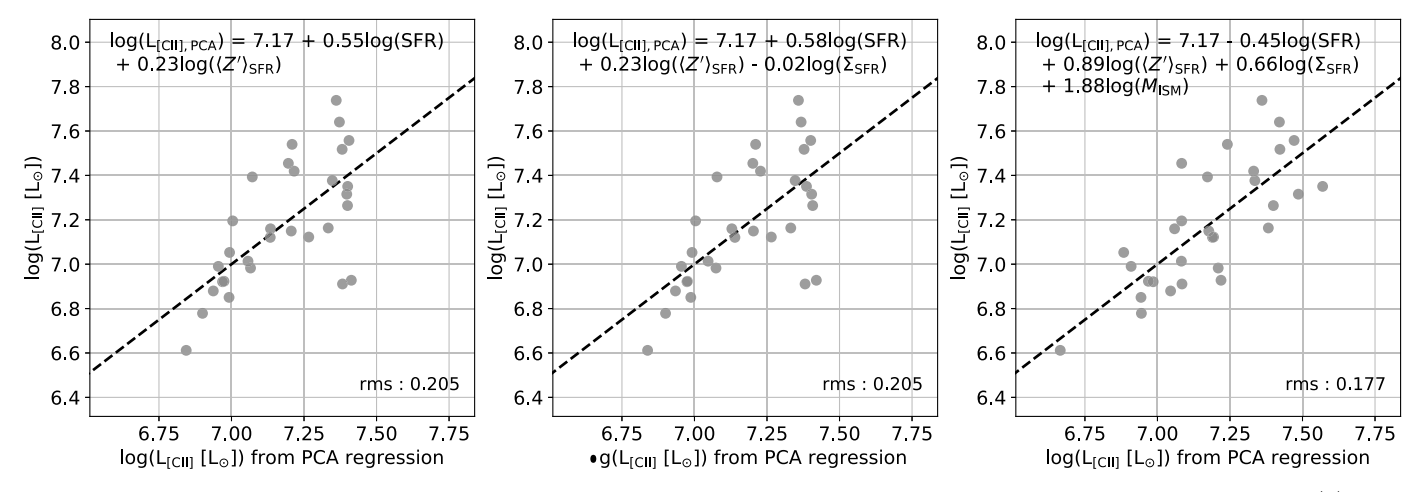


Figure 10. Results of a PCA regression to the [C II] luminosities of our simulations using different sets of free parameters. Left panel: SFR and $\langle Z \rangle_{SFR}$ (see Equation (13)). Middle panel: SFR, $\langle Z \rangle_{SFR}$, and Σ_{SFR} (see Equation (12)). Right panel: SFR, Σ_{SFR} , and Σ_{SFR} (see Equation (11)). The dashed lines indicate the 1:1 line. The rms scatter of the simulations with respect to Equations (11)–(13) is indicated.

2017). However, recent studies at high redshifts have shown that dust production is less efficient at low metallicities, resulting in DTM mass ratios significantly below that of the MW in low-metallicity systems (Vladilo 2004; De Cia et al. 2013, 2016; Wiseman et al. 2017).

We ran SÍGAME using new grids of CLOUDY models with a DTM ratio of 0.25, i.e., half of that adopted in Section 3.3. The effect is to increase the [C II] luminosities of the simulated galaxies by $\sim\!43\%$ on average, or 0.15 dex, and the change to the $L_{\rm [C II]}$ – SFR relation is therefore significant (Figure 11, left panel). The increase in $L_{\rm [C II]}$ is primarily coming from the GMCs, where decreasing the amount of dust reduces the shielding of the gas from FUV radiation, thereby allowing for larger C⁺ envelopes.

The GMC mass distribution. In high-z environments, the GMCs are likely to differ from the Galactic mass spectrum (slope $\beta=1.8$), which was adopted for our simulations (Section 3.1). In our Local Group alone, where GMC masses can be measured, significant variations in β have been found: from $\beta=1.5$ in the inner MW, to $\beta=2.1$ and $\beta=2.9$ in the outer MW and in M33, respectively (Rosolowsky 2005; Blitz et al. 2007). Running SÍGAME with a "bottom-heavy" ($\beta=3.0$) GMC mass spectrum has practically no impact on

the [C II] emission of the galaxies, but switching to a "topheavy" ($\beta=1.5$) GMC mass spectrum increases $L_{\rm [C II]}$ by an average of 44% or 0.15 dex (Figure 11, middle panel), similar to the case of reduced DTM ratio.

Abundances. As we saw in Section 3.3, SÍGAME ascribes to a cloud (dense or diffuse) the element abundances of the local ISM, but scaled by the metallicity of the parent fluid element. This ensures a one-to-one relation between the abundance of an element and the metallicity, which is required in order to keep the number of CLOUDY models at a manageable level. These relations (one for each element) can easily be converted to relations between element mass fractions and metallicity, and are plotted (green dashed–dotted lines) in Figure 12, which shows the element mass fractions against metallicity for the fluid elements in three of the MUFASA galaxy simulations. It is seen that this approach does not match the element mass fractions of the simulations particularly well.

As a result, we devised an alternative approach that would ensure that the element abundances provided as input to CLOUDY did in fact reflect the typical element mass fractions in the MUFASA simulations. In this approach, a one-to-one relation between the mass fraction of an element and the metallicity is established by simply doing spline fits to the

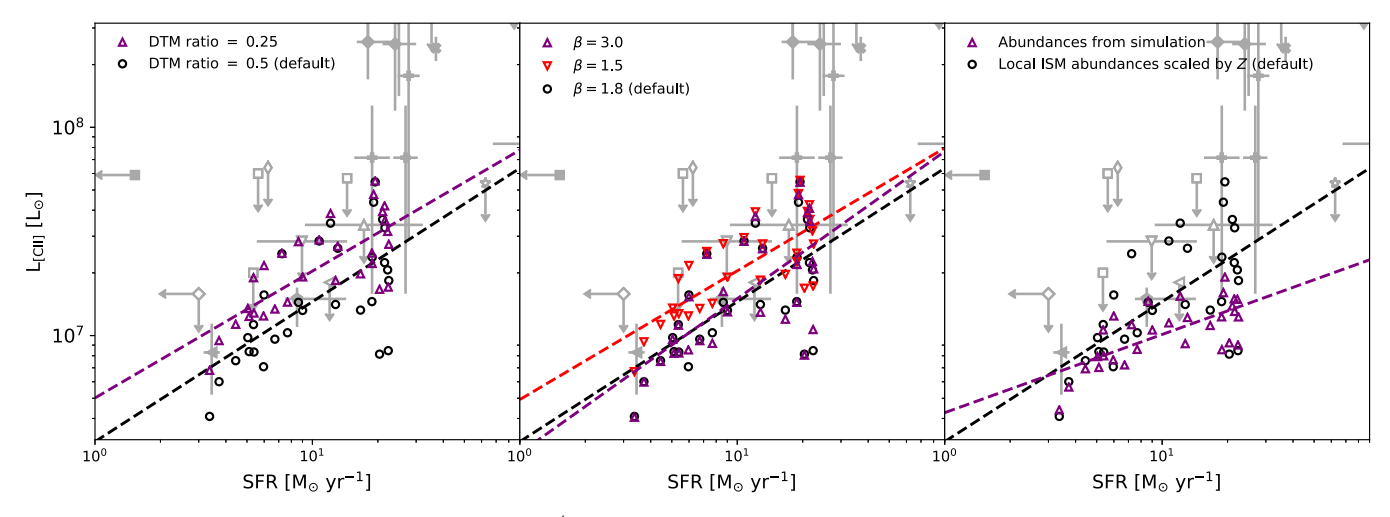


Figure 11. Result of deviating from the default assumptions of SÍGAME. Purple triangles show the simulated galaxies in the $L_{[C II]}$ -SFR diagram after reducing the DTM ratio by a factor of 2 (left), changing the GMC mass spectrum to one that is more bottom heavy or top heavy (middle), and adopting abundances that better match the cosmological simulation (right). Black circles show the location of model galaxies with the default assumptions of SÍGAME. Observations are shown with gray symbols as in Figure 6.

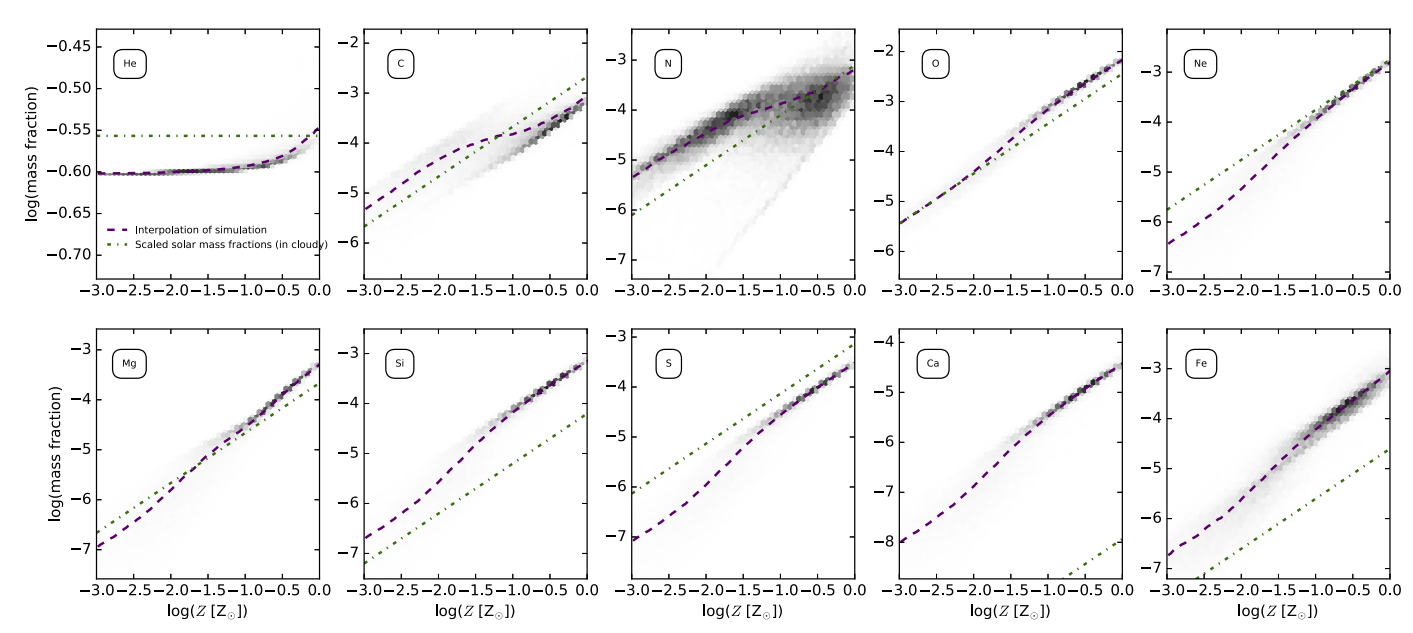


Figure 12. Gray contours represent the mass fractions of the elements tracked in the MUFASA simulation set as function of the metallicity of individual fluid elements for a subsample of three randomly selected model galaxies used in this work. Using the local ISM abundances stored in CLOUDY and scaled by metallicity gives the green dashed—dotted line. These are our default abundances in SÍGAME for this project. We also make a grid of cloudy models in which each element shown here is scaled to match the simulation as represented by the purple dashed lines, which consist of running the means of the values of the gas fluid elements.

average mass fractions within 100 bins in metallicity (purple dashed curve in Figure 12). It is then straightforward to infer the corresponding element abundances (as a function of metallicity). Adopting this approach tends to lower the [C II] luminosities of our simulations, although in some cases there is actually a very slight increase. The net outcome is a shallower $L_{\rm [C II]}$ –SFR relation (Figure 11, right panel), but one that remains consistent with the [C II]-faint observations. The lower [C II] luminosities are due to the fact that over the metallicity range spanning the majority of both dense and diffuse clouds in the simulations ($-1.5 \lesssim \log Z/Z_{\odot} \lesssim 0$; Figures 4 and 5), the default local ISM abundances (green dashed–dotted lines) overshoot the average simulation carbon abundances (purple dashed curves).

5.2. Reconciling [CII]-luminous Sources at $z \sim 6$ with our Simulations

In the previous section, we saw that our simulation findings are relatively robust against changes in some of the model assumptions. In particular, we saw that it is difficult to increase the [C II] emission from the simulations. This then begs the question of how to account for the [C II]-luminous LBGs detected by Capak et al. (2015), Willott et al. (2015), and Smit et al. (2017) as well as the luminous QSO companions detected by Decarli et al. (2017), which all lie significantly above the $L_{\rm [C II]}$ -SFR relation defined by our simulations and the many [C II]-faint sources (e.g., Maiolino et al. 2015; Bradač et al. 2017).

Observational uncertainties. The SFRs of galaxies at $z\sim 6$ are derived via either conversion from IR luminosities or restframe UV continuum luminosities (corrected for dust). Although there can be significant uncertainties associated with estimating the SFRs of high-z galaxies, in the case of the Capak et al. (2015) and Willott et al. (2015) LBGs, they would have had to be underestimated by an order of magnitude if this were the reason for the above discrepancy. Capak et al. (2015) estimate a systematic uncertainty of 0.3 dex on the IR luminosities, which are inferred from only a single long-wavelength ($\lambda_{\rm obs} = 0.85-1$ mm) data point and scaling a modified blackbody law to it with dust temperatures in the range 25–45 K, spectral indices of 1.2–2.0, and Wien power-law slopes of 1.5–2.5.

We made an estimate of the dust temperatures in our model galaxies using the dust radiative transfer package powderday (Narayanan et al. 2015, 2017) to generate dust emission SEDs for the central halos from which we extract galaxies. powderday builds off of HYPERION (Robitaille 2011; Robitaille et al. 2012), FSPS (Conroy et al. 2009, 2010), and YT (Turk et al. 2011). In short, powderday generates stellar spectra for all of the stars formed in the simulation using their ages and metallicites, and computes their SEDs as simple stellar populations using FSPS. The metal properties of the model galaxies are projected onto an adaptive grid with an octree memory structure using YT, and then the stellar SEDs are propagated through the dusty ISM using HYPERION as the dust radiative transfer solver. This process is iterated upon in a Monte Carlo fashion until the radiation field and dust temperatures achieve equilibrium. Since we only extract central galaxies, these SEDs will be dominated by the light from our simulated galaxies. The resulting dust temperatures lie in the range 50-72 K, i.e., significantly warmer than the Capak et al. (2015) sources. If >50 K is a more appropriate temperature range for the dust in $z \sim 6$ LBGs, it would imply that their IR luminosities have been underestimated. Whether this also implies higher star formation rates is less clear. We note that this is a good bit warmer than the typical dust temperature of simulations of comparable luminosity galaxies at $z \sim 0$ –2 (e.g., Narayanan et al. 2010, 2011); this is due principally to the low dust contents and hard radiation fields in low-metallicity galaxies at z > 5.

AGNs. The possibility that the [C II]-brightness of the Capak et al. (2015) and Willott et al. (2013) sources could be due to the presence of AGNs seems unlikely since normal LBGs at $z \sim 6$ are expected to have moderate-mass black holes ($\lesssim 10^8 \, M_\odot$) that would not dominate the overall energetics. Also, [C II] observations of QSOs at $z \sim 6$ (and at lower redshifts) tend to show lower, not higher, $L_{\rm [CII]}/L_{\rm IR}$ values compared to star-forming galaxies (Maiolino et al. 2005; Venemans et al. 2012; Wang et al. 2013; Zhao et al. 2016).

Gas mass fractions. Is it possible that our simulations and the [C II]-faint sources have significantly lower gas mass fractions, and thus smaller gas reservoirs that can emit in [C II], than the [C II]-bright LBGs? In Section 4.2, we found that the molecular and diffuse ionized gas phases contribute about equally to the total [C II] luminosities of simulations with SFR $\lesssim 10~M_{\odot}~yr^{-1}$, while at higher SFRs the ionized gas tends to dominate. Taking these findings at face value would suggest that the [C II]-bright LBGs may have higher fractions of either ionized or molecular gas, or both, than our simulations and [C II]-faint sources.

To investigate this, we first show in Figure 13 the molecular gas mass fractions $(f_{\rm mol})$ of our simulated galaxies as calculated

directly from Table 1. The molecular gas mass fractions decrease with SFR, going from ~ 0.6 at the lowest SFR to ~ 0.1 at the highest SFRs (red filled circles in Figure 13). For the Capak et al. (2015) and Willott et al. (2015) LBGs, we do not have direct estimates of their gas mass fractions. Instead, we apply to them the parametrizations provided by Scoville et al. (2016), which give f_{mol} as a function of z, M_* , and SFR (and denominated $f_{\text{mol},S16}$ in the figure). The resulting fractions for the LBGs, shown as green diamonds and crosses in Figure 13, are significantly higher ($f_{\rm mol,S16} \sim 0.4$ –0.6) than those of our simulations at SFR $~\gtrsim~10~M_{\odot}~{
m yr}^{-1}~(f_{
m mol}~\sim~0.1).$ Applying the same parametrizations to our simulated galaxies yields $f_{
m mol,S16} \sim 0.4$, which matches well with the Capak et al. (2015) and Willott et al. (2015) sources. This would mean roughly $4\times$ higher $f_{\rm mol}$ at the highest SFRs of our models, which translates into a $6\times$ higher molecular gas mass for a fixed stellar mass. For comparison, we also show the ionized gas mass fractions, f_{ion} , of our model galaxies, which at present cannot be compared to the $z \sim 5-6$ LBGs of Capak et al. (2015) and Willott et al. (2015), but we note a decrease in f_{ion} with SFR similar to that of $f_{\rm mol}$.

In adopting the relation from Scoville et al. (2016), we are making three major assumptions: (1) that the relation created from galaxies out to z=5.89 can be extrapolated to $z\sim 6$, (2) that M_* and SFR are derived in similar fashions from observations as from our simulations, and (3) that the actual molecular gas masses in our simulations correspond to the dust-derived molecular ISM masses used in Scoville et al. (2016). However, if all of these assumptions are valid, then it implies that the range of $f_{\rm mol}$ in our model galaxies does not reach the higher $f_{\rm mol}$ values derived for observed galaxies close to z=6. This will tend to make our models underpredict the [C II] emission since we find that the [C II] efficiency of molecular regions is generally higher than that of diffuse regions of the ISM (cf. Figure 7).

Metallicities. In Section 4.4, we saw that simulations with higher average metallicities also tend to have higher [C II] luminosities (Figure 9 and Equation (11)). Our simulations all have metallicities well below solar ($\langle Z \rangle_{SFR} \lesssim 0.45$)—and less than half the metallicity of the local metal-poor dwarf galaxies studied by De Looze et al. (2014)—which may therefore partly account for their [C II] faintness and the discrepancy with the Capak et al. (2015) sources, which are likely to have higher metallicities.

Figure 14 shows the [C II]-SFR relation obtained when scaling the metallicities of our simulations by a factor of three, leading to SFR-weighted metallicities of 0.4 to 1.4 solar and a mass-metallicity relation for our model galaxies close to that observed at $z \sim 1.3$ –2.3 for galaxies of similar masses (Erb et al. 2006; Henry et al. 2013; Sanders et al. 2015). This is therefore an extreme case, in which our $z \sim 6$ galaxies have already achieved typical metallicities at $z \sim 1.3-2.3$. In order to test this case, new CLOUDY grids were calculated for both the dense and diffuse gas. The net effect of raising the metallicities is to increase the [C II] luminosities of our simulations by 0.4 dex on average, thereby bringing them better in line with the [C II] detections of Capak et al. (2015) at SFR $\sim 20 \ M_{\odot} \ yr^{-1}$. This picture is consistent with the relatively low Lylpha line strength measured for the $z\sim5$ -6 detections (Capak et al. 2015; Willott et al. 2015; Pentericci et al. 2016), since the Ly α strength decreases with the dust amount and hence metallicity (e.g., Pirzkal et al. 2007; Yang

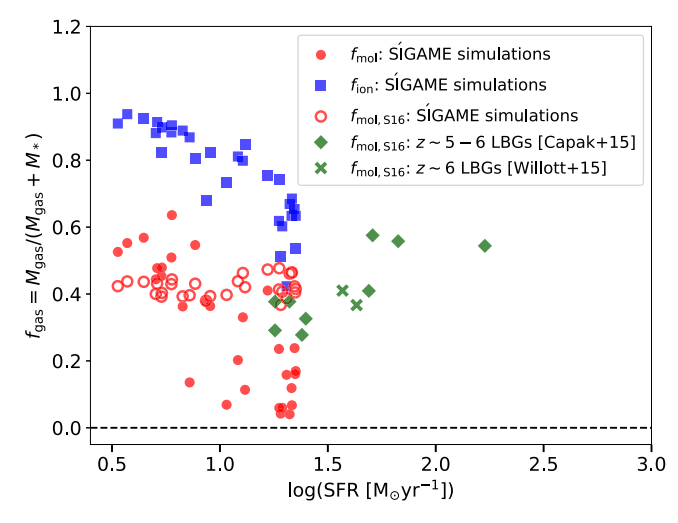


Figure 13. Molecular gas mass fractions of our simulations and of the $z\sim5$ –6 LBGs observed by Capak et al. (2015) and Willott et al. (2015). The filled and open red circles indicate true fractions inferred directly from the simulations and fractions inferred from the parametrizations in Scoville et al. (2016), respectively. Applying this parametrization to the $z\sim5$ –6 LBGs gives the molecular gas mass fractions shown by the green diamonds and crosses. Also shown are the true ionized gas mass fraction of our simulations (blue filled squares).

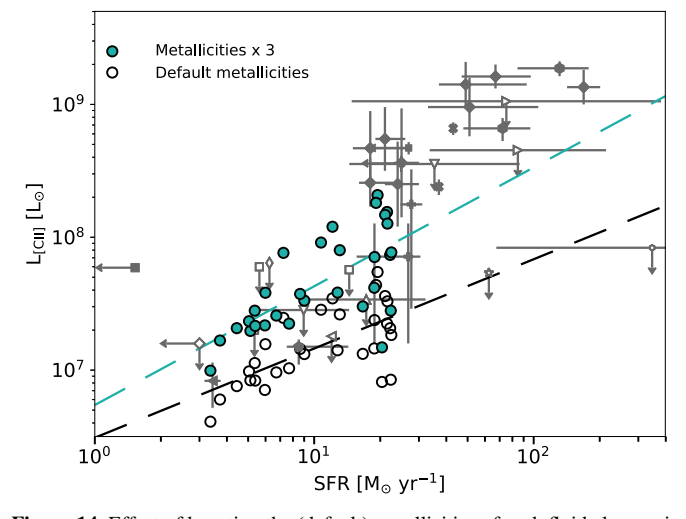


Figure 14. Effect of boosting the (default) metallicities of each fluid element in our simulations by a factor of three results in galaxy [C II] luminosities (filled cyan circles) that are on average ~ 2.5 –3× higher. Even so, this does not bring the simulations fully into accord with the [C II]-bright detections at $z \simeq 6$, although there is an overlap with observations for some simulations. The dashed cyan line shows the log-linear fit to the simulations with high metallicities.

et al. 2017), except in cases where the ISM is very inhomogeneous (e.g., Giavalisco et al. 1996; though see also the model results by Laursen et al. 2013).

We note that the ~ 0.4 dex increase in the [C II] luminosity of our simulations is mainly coming from the neutral and diffuse ionized gas, where an increase in the metallicity results in a higher abundance of C⁺. For the GMCs, an increase in the metallicity results in a higher degree of UV attenuation by dust and therefore thinner C⁺ layers. This is the same effect we saw in Figure 7 where the fraction of the total [C II] luminosity coming from GMCs decreases with increasing metallicity of the simulations.

6. Conclusion

We have applied an updated version of SÍGAME to MUFASA simulations in order to model the [C II], [O I], and [O III] line emission from $z\sim 6$ galaxies on the main sequence with stellar masses $\sim (0.7-8)\times 10^9\,M_\odot$ and metallicities $\sim (0.1-0.4)\times Z_\odot$.

The simulations are able to reproduce observations of [C II]-faint star-forming galaxies at $z \gtrsim 5$ —i.e., galaxies with [C II] luminosities (many of which are upper limits) that are $\sim 6-32 \times$ lower than expected from local $L_{\rm [C II]}$ -SFR relations and from samples of [C II]-bright galaxies at $z \sim 5-6$ (Capak et al. 2015; Willott et al. 2015). Extrapolating a log-linear fit to our simulations to higher SFRs ($\sim 50-300~{\rm M}_{\odot}~{\rm yr}^{-1}$) results in agreement with observations of [C II]-faint galaxies at these higher SFRs.

The [O I] and [O III] luminosities from the simulated galaxies are in broad agreement with the $L_{\rm [O I]}$ -SFR and $L_{\rm [O III]}$ -SFR relations of local starburst galaxies (De Looze et al. 2014), as well as with two of the three existing $z \gtrsim 5$ detections of [O III] to date (Inoue et al. 2016; Laporte et al. 2017).

Dividing the [C II] luminosities of our simulations into contributions from the different ISM phases, we find that the [C II] emission predominantly comes from the diffuse ionized gas and the GMCs, which, on average contribute $\sim\!66\%$ and $\sim\!27\%$, respectively, while the diffuse neutral phase contributes $\sim\!7\%$. In terms of mass, the three phases constitute on average $\sim\!85\%$, $\sim\!10\%$, and $\sim\!10\%$ of the total ISM mass in our simulations. Thus, the GMCs are the most efficient [C II] emitters of the ISM phases, suggesting that the molecular gas fraction plays a role in whether a galaxy is [C II] faint or [C II] bright.

A principal component analysis shows that $L_{[C \ II]}$ primarily depends on $\Sigma_{\rm SFR}$ and SFR. Furthermore, including metallicity in the set of free global parameters reduces the scatter between the $L_{[C \ II]}$ from the PCA parametrization and the $L_{[C \ II]}$ from the simulations. In our models, the ISM mass is not an important parameter in setting $L_{[C \ II]}$.

The modeling presented in this paper suggests that the [C II]-faint $z \gtrsim 5$ main-sequence galaxies, including [C II] non-detections, are likely the result of low metallicities and low molecular gas fractions. More observations of FIR emission lines at high redshift together with more precise SFR determinations are needed in order to compare better with models such as ours, yet at the same time we have to work toward modeling galaxies with a more dynamic range in physical parameters such as metallicity and SFR.

The authors thank the anonymous referee for a careful reading of the manuscript and insightful comments that greatly improved the quality of this work. The authors thank Sangeeta Malhotra and Kristian Finlator for fruitful discussions. The authors acknowledge the Texas Advanced Computing Center (TACC) at The University of Texas at Austin for providing high performance computing resources that have contributed to the research results reported in this paper (http://www.tacc.utexas.edu). In addition, this work benefited from resources provided by the NASA High-End Computing (HEC) Program through the NASA Advanced Supercomputing (NAS) Division, and from computational resources and technical expertise provided by ASU Research Computing, Tempe, Arizona. The hydrodynamic simulations published here were run on the University of Florida HiPerGator facility, and the authors

acknowledge the University of Florida Research Computing for providing computational resources and support that have contributed to the research results reported in this publication. Partial support for D.N. was provided by AST-1715206, AST-1724864, NASA HST AR-13906.001 from the Space Telescope Science Institute, which is operated by the Association of University for Research in Astronomy, Incorporated, under NASA Contract NAS5-26555, and a Cottrell College Science Award, awarded by the Research Corporation for Science Advancement.

ORCID iDs

Karen Olsen https://orcid.org/0000-0003-1250-5287 Thomas R. Greve https://orcid.org/0000-0002-2554-1837 Desika Narayanan https://orcid.org/0000-0002-7064-4309 Romeel Davé https://orcid.org/0000-0003-2842-9434 Stephanie Stawinski https://orcid.org/0000-0001-8169-7249

References

```
Accurso, G., Saintonge, A., Bisbas, T. G., & Viti, S. 2017, MNRAS, 464, 3315
Asplund, M., Grevesse, N., Sauval, A. J., & Scott, P. 2009, ARA&A, 47, 481
Blitz, L., Fukui, Y., Kawamura, A., et al. 2007, in Protostars and Planets V, ed.
  B. Reipurth, D. Jewitt, & K. Keil (Tucson, AZ: Univ. Arizona Press), 81
Bonato, M., Negrello, M., Cai, Z.-Y., et al. 2014, MNRAS, 438, 2547
Bradač, M., Garcia-Appadoo, D., Huang, K.-H., et al. 2017, ApJL, 836, L2
Brauher, J. R., Dale, D. A., & Helou, G. 2008, ApJS, 178, 280
Bruzual, G., & Charlot, S. 2003, MNRAS, 344, 1000
Capak, P. L., Carilli, C., Jones, G., et al. 2015, Natur, 522, 455
Carniani, S., Maiolino, R., Pallottini, A., et al. 2017, arXiv:1701.03468
Chabrier, G. 2003, PASP, 115, 763
Chomiuk, L., & Povich, M. S. 2011, AJ, 142, 197
Conroy, C., Gunn, J. E., & White, M. 2009, ApJ, 699, 486
Conroy, C., White, M., & Gunn, J. E. 2010, ApJ, 708, 58
Cormier, D., Lebouteiller, V., Madden, S. C., et al. 2012, A&A, 548, A20
Davé, R., Rafieferantsoa, M. H., Thompson, R. J., & Hopkins, P. F. 2017,
          S. 467, 115
Davé, R., Thompson, R., & Hopkins, P. F. 2016, MNRAS, 462, 3265
De Cia, A., Ledoux, C., Mattsson, L., et al. 2016, A&A, 596, A97
De Cia, A., Ledoux, C., Savaglio, S., Schady, P., & Vreeswijk, P. M. 2013,
       A, 560, A88
De Looze, I., Cormier, D., Lebouteiller, V., et al. 2014, A&A, 568, A62
Decarli, R., Walter, F., Venemans, B. P., et al. 2017, Natur, 545, 457
Díaz-Santos, T., Armus, L., Charmandaris, V., et al. 2013, ApJ, 774, 68
Diaz-Santos, T., Armus, L., Charmandaris, V., et al. 2017, arXiv:1705.04326
Draine, B. T. 2011, Physics of the Interstellar and Intergalactic Medium
   (Princeton, NJ: Princeton Univ. Press)
Erb, D. K., Shapley, A. E., Pettini, M., et al. 2006, ApJ, 644, 813
Ferkinhoff, C., Hailey-Dunsheath, S., Nikola, T., et al. 2010, ApJL, 714, L147
Ferland, G. J., Chatzikos, M., Guzmán, F., et al. 2017, arXiv:1705.10877
Ferland, G. J., Porter, R. L., van Hoof, P. A. M., et al. 2013, RxMAA, 49, 137
Fischer, J., Luhman, M. L., Satyapal, S., et al. 1999, Ap&SS, 266, 91
Giavalisco, M., Koratkar, A., & Calzetti, D. 1996, ApJ, 466, 831
Goldsmith, P. F., Langer, W. D., Pineda, J. L., & Velusamy, T. 2012, ApJS,
González-López, J., Riechers, D. A., Decarli, R., et al. 2014, ApJ, 784, 99
Gullberg, B., De Breuck, C., Vieira, J. D., et al. 2015, MNRAS, 449, 2883
Hahn, O., & Abel, T. 2011, MNRAS, 415, 2101
Hayward, C. C., & Smith, D. J. B. 2015, MNRAS, 446, 1512
Helou, G., Malhotra, S., Hollenbach, D. J., Dale, D. A., & Contursi, A. 2001,
Henry, A., Scarlata, C., Domínguez, A., et al. 2013, ApJL, 776, L27
Herrera-Camus, R., Bolatto, A. D., Wolfire, M. G., et al. 2015, ApJ, 800, 1
Hopkins, P. F. 2015, MNRAS, 450, 53
Inoue, A. K., Tamura, Y., Matsuo, H., et al. 2016, Sci, 352, 1559
Iwamoto, K., Brachwitz, F., Nomoto, K., et al. 1999, ApJS, 125, 439
Jiang, L., Finlator, K., Cohen, S. H., et al. 2016, ApJ, 816, 16
Jolliffe, I. 2002, Principal Component Analysis (New York: Springer)
Kanekar, N., Wagg, J., Ram Chary, R., & Carilli, C. L. 2013, ApJL, 771, L20
Kapala, M. J., Sandstrom, K., Groves, B., et al. 2015, ApJ, 798, 24
```

```
Katz, H., Kimm, T., Sijacki, D., & Haehnelt, M. G. 2017, MNRAS, 468, 4831
Kennicutt, R. C., & Evans, N. J. 2012, ARA&A, 50, 531
Knudsen, K. K., Richard, J., Kneib, J.-P., et al. 2016, MNRAS, 462, L6
Knudsen, K. K., Watson, D., Frayer, D., et al. 2017, MNRAS, 466, 138
Krumholz, M. R., & Gnedin, N. Y. 2011, ApJ, 729, 36
Krumholz, M. R., McKee, C. F., & Tumlinson, J. 2009, ApJ, 693, 216
Laporte, N., Ellis, R. S., Boone, F., et al. 2017, ApJL, 837, L21
Laursen, P., Duval, F., & Östlin, G. 2013, ApJ, 766, 124
Leitherer, C., Ekström, S., Meynet, G., et al. 2014, ApJS, 212, 14
Luhman, M. L., Satyapal, S., Fischer, J., et al. 1998, ApJL, 504, L11
Luhman, M. L., Satyapal, S., Fischer, J., et al. 2003, ApJ, 594, 758
Maiolino, R., Carniani, S., Fontana, A., et al. 2015, MNRAS, 452, 54
Maiolino, R., Cox, P., Caselli, P., et al. 2005, A&A, 440, L51
Malhotra, S., Helou, G., Stacey, G., et al. 1997, ApJL, 491, L27
Malhotra, S., Kaufman, M. J., Hollenbach, D., et al. 2001, ApJ, 561, 766
Muñoz, J. A., & Furlanetto, S. R. 2014, MNRAS, 438, 2483
Muratov, A. L., Kereš, D., Faucher-Giguère, C.-A., et al. 2015, MNRAS,
  454, 2691
Narayanan, D., Dave, R., Johnson, B., et al. 2017, arXiv:1705.05858
Narayanan, D., Dey, A., Hayward, C. C., et al. 2010, MNRAS, 407, 1701
Narayanan, D., Krumholz, M., Ostriker, E. C., & Hernquist, L. 2011, MNRAS,
Narayanan, D., & Krumholz, M. R. 2017, MNRAS, 467, 50
Narayanan, D., Turk, M., Feldmann, R., et al. 2015, Natur, 525, 496
Nomoto, K., Tominaga, N., Umeda, H., Kobayashi, C., & Maeda, K. 2006,
   NuPhA, 777, 424
Olsen, K. P., Greve, T. R., Narayanan, D., et al. 2015, ApJ, 814, 76
Oppenheimer, B. D., & Davé, R. 2008, MNRAS, 387, 577
Ota, K., Walter, F., Ohta, K., et al. 2014, ApJ, 792, 34
Ouchi, M., Ellis, R., Ono, Y., et al. 2013, ApJ, 778, 102
Pallottini, A., Ferrara, A., Gallerani, S., et al. 2017, MNRAS, 465, 2540
Papadopoulos, P. P., Thi, W.-F., Miniati, F., & Viti, S. 2011, MNRAS,
  414, 1705
Papadopoulos, P. P., Zhang, Z.-Y., Xilouris, E. M., et al. 2014, ApJ, 788, 153
Pentericci, L., Carniani, S., Castellano, M., et al. 2016, ApJL, 829, L11
Pineda, J. L., Langer, W. D., & Goldsmith, P. F. 2014, A&A, 570, A121
Pirzkal, N., Malhotra, S., Rhoads, J. E., & Xu, C. 2007, ApJ, 667, 49
Planck Collaboration, Ade, P. A. R., Aghanim, N., et al. 2016, A&A, 594, A13
Popping, G., van Kampen, E., Decarli, R., et al. 2016, MNRAS, 461, 93
Rahmati, A., Pawlik, A. H., Raičevic', M., & Schaye, J. 2013, MNRAS,
  430, 2427
Rigopoulou, D., Hopwood, R., Magdis, G. E., et al. 2014, ApJL, 781, L15
Robitaille, T. P. 2011, A&A, 536, A79
Robitaille, T. P., Churchwell, E., Benjamin, R. A., et al. 2012, A&A, 545, A39
Röllig, M., Ossenkopf, V., Jeyakumar, S., Stutzki, J., & Sternberg, A. 2006,
    &A. 451, 917
Rosenberg, M. J. F., van der Werf, P. P., Aalto, S., et al. 2015, ApJ, 801, 72
Rosolowsky, E. 2005, PASP, 117, 1403
Sanders, R. L., Shapley, A. E., Kriek, M., et al. 2015, ApJ, 799, 138
Sargsyan, L., Samsonyan, A., Lebouteiller, V., et al. 2014, ApJ, 790, 15
Schaerer, D., Boone, F., Zamojski, M., et al. 2015, A&A, 574, A19
Schmidt, M. 1959, ApJ, 129, 243
Scoville, N., Sheth, K., Aussel, H., et al. 2016, ApJ, 820, 83
Seon, K.-I., Edelstein, J., Korpela, E., et al. 2011, ApJS, 196, 15
Smit, R., Bouwens, R. J., Carniani, S., et al. 2017, arXiv:1706.04614
Smith, J. D. T., Croxall, K., Draine, B., et al. 2017, ApJ, 834, 5
Somerville, R. S., & Davé, R. 2015, ARA&A, 53, 51
Speagle, J. S., Steinhardt, C. L., Capak, P. L., & Silverman, J. D. 2014, ApJS,
  214, 15
Springel, V. 2005, MNRAS, 364, 1105
Stacey, G. J., Geis, N., Genzel, R., et al. 1991, ApJ, 373, 423
Stacey, G. J., Hailey-Dunsheath, S., Ferkinhoff, C., et al. 2010, ApJ, 724, 957
Sturm, E., Verma, A., Graciá-Carpio, J., et al. 2010, A&A, 518, L36
Turk, M. J., Smith, B. D., Oishi, J. S., et al. 2011, ApJS, 192, 9
Vallini, L., Gallerani, S., Ferrara, A., & Baek, S. 2013, MNRAS, 433, 1567
Vallini, L., Gallerani, S., Ferrara, A., Pallottini, A., & Yue, B. 2015, ApJ,
Venemans, B. P., McMahon, R. G., Walter, F., et al. 2012, ApJL, 751, L25
Vladilo, G. 2004, A&A, 421, 479
Wang, R., Wagg, J., Carilli, C. L., et al. 2013, ApJ, 773, 44
Webber, W. R. 1998, ApJ, 506, 329
Willott, C. J., Carilli, C. L., Wagg, J., & Wang, R. 2015, ApJ, 807, 180
Willott, C. J., Omont, A., & Bergeron, J. 2013, ApJ, 770, 13
Wiseman, P., Schady, P., Bolmer, J., et al. 2017, A&A, 599, A24
Yang, H., Malhotra, S., Gronke, M., et al. 2017, ApJ, 844, 171
Zhao, Y., Yan, L., & Tsai, C.-W. 2016, ApJ, 824, 146
```



Erratum: "SÍGAME Simulations of the [CII], [OI], and [OIII] Line Emission from Star-forming Galaxies at $z \simeq 6$ " (2017, ApJ, 846, 105)

Karen Olsen¹, Thomas R. Greve², Desika Narayanan³, Robert Thompson⁴, Romeel Davé^{5,6,7},

Luis Niebla Rios¹, and Stephanie Stawinski¹

School of Earth and Space Exploration, Arizona State University, 781 South Terrace Road, Tempe, AZ 85287, USA; kpolsen@asu.edu

Department of Physics and Astronomy, University College London, Gower Street, London WC1E 6BT, UK

Department of Astronomy, University of Florida, 211 Bryant Space Sciences Center, Gainesville, FL, USA

Portalarium, Austin, TX 78731, USA

University of the Western Cape, Bellville, Cape Town 7535, South Africa
 South African Astronomical Observatory, Observatory, Cape Town 7925, South Africa
 Institute for Astronomy, Royal Observatory, Edinburgh EH9 3HJ, UK
 Received 2018 January 2; revised 2018 March 28; published 2018 April 25

1. Accounting for the CMB with CLOUDY

Due to an oversight on our part, the published line emissions were not corrected for the effects of the cosmic microwave background (CMB). It is well known that at $z \sim 6$, the temperature of the CMB is sufficiently high to pump the [C II] level population, and line emission from gas clouds is observed in contrast against the CMB (e.g., Chatzikos et al. 2013). We mistakenly used an output from CLOUDY that did not account for the CMB. To rectify this, we now use the CLOUDY output *emergent intensity*, for which the CMB radiative coupling to the gas and the CMB background subtraction have been taken into account. The result is a slight decrease in the line emission of the model galaxies, bringing our results on [C II]-contributing ISM phases into better agreement with similar simulation studies and the observed [C II] observations of the Milky Way. We now find that the [C II] emission is dominated by the molecular clouds and diffuse ionized gas, which, on average, contribute $\sim 50\%$ and $\sim 44\%$, respectively.

2. Geometrical Correction

In addition to the CMB correction, we also take this opportunity to apply a purely geometrical correction to our previously published intensities. This is because in CLOUDY the intensity is calculated for a plane–parallel geometry (a slab), while in SÍGAME the clouds are assumed to be spherical. Below we outline the derivation of such approximate correction factors, which were calculated on a cloud-per-cloud basis and subsequently applied to the emergent intensity from CLOUDY.

Simply multiplying the emergent intensity by the surface area of the spherical cloud results in an overestimation of the emergent luminosity, because the slabs used in a plane–parallel geometry will overlap, as illustrated in Figure 1(a). By using pyramids with bases at the surface of the cloud and tops at the cloud center, we can circumvent this problem, as shown in Figure 1(b). The volume of the sphere can be approximately covered by an infinite number of such pyramid-shaped volume elements.

We will calculate an intrinsic line intensity (not corrected for the CMB) for a pyramid-shaped volume element of base area equal to that of the slab and denote it as $I_{\text{int,pyra}}$. The goal in the following is to calculate the equivalent emergent intensity, $I_{\text{em,pyra}}$ (which has been corrected for the CMB). To achieve this goal, we define the following quantities:

- 1. The emergent line intensity for a slab (with units erg cm⁻² s⁻¹), which we will denote as $I_{em,slab}$. This quantity has been corrected for CMB.
- 2. The intrinsic line intensity for a slab (with units erg cm⁻² s⁻¹), which we will denote as $I_{int,slab}$. This quantity is not corrected for CMB
- 3. The volume line emissivity (with units erg cm⁻³ s⁻¹), which we will denote as $\Lambda(R)$ since it has the same units as cooling rate. This quantity is also not corrected for CMB.

If CMB is not included in the radiation field used by CLOUDY, then $I_{\rm em,slab}$ is equal to $I_{\rm int,slab}$ which is equal to the integral over $\Lambda(R)$ from cloud center to cloud surface:

$$I_{\rm em,slab} = I_{\rm int,slab} = \int_0^{R_{\rm cloud}} \Lambda(R) dR'. \tag{1}$$

Integrating $\Lambda(R)$ over a pyramid with base area 1 cm² and height R_{cloud} can be shown to give

$$I_{\text{int,pyra}} = \int_0^{R_{\text{cloud}}} \Lambda(R) (R'/R_{\text{cloud}})^2 dR'.$$
 (2)

In the case in which $\Lambda(R)$ is a constant as a function of radius, which is often the case in our diffuse clouds, Equations (1) and (2) simplify to

$$I_{\text{int,slab}} = \Lambda(R)R_{\text{cloud}}$$
 and $I_{\text{int,pvra}} = 1/3 \Lambda(R)R_{\text{cloud}}$. (3)

Meaning that the emergent intensities need to be corrected by a geometrical correction factor of 1/3, before the integration over cloud surface area to get the correct luminosity for a spherical cloud. If $\Lambda(R)$ varies as a function of radius, then this correction factor

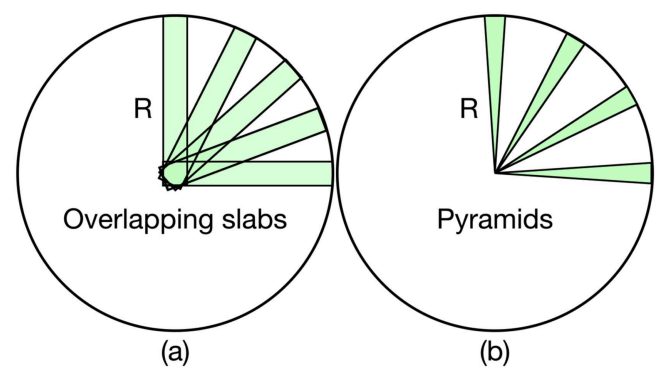


Figure 1. Illustrations of the choice of volume element to fill up a spherical cloud, where (a) shows slabs of constant width, overlapping in the central regions and (b) shows pyramids that are not overlapping. In case (b), these pyramids can be used to trace the entire volume of the sphere.

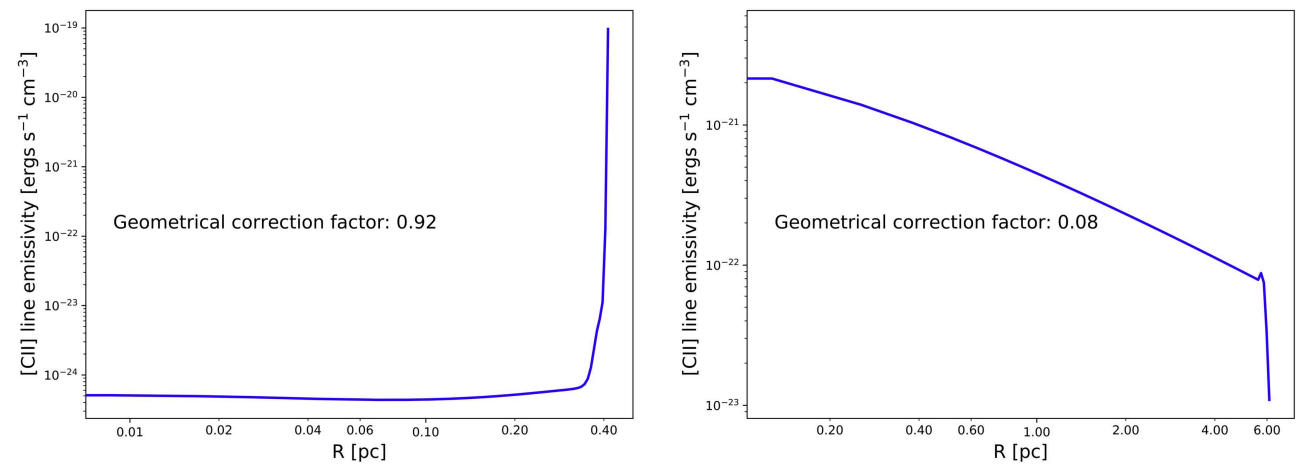


Figure 2. Left: radial profile of $\Lambda(R)$ in the cloud model with the highest geometrical correction factor. This cloud model is a GMC of radius 0.4 pc, mass $10^{4.28}~M_{\odot}$, $P_{\rm ext}=10^{9.1}~{\rm K~cm^{-3}}$, metallicity $10^{-1.64}~Z_{\odot}$, and irradiated by a G_0 of $10^{0.80}\langle G_0\rangle$. Right: same, but for the cloud model with the lowest geometrical correction factor. This cloud model is also a GMC, but with radius 6.1 pc, mass $10^{4.82}~M_{\odot}$, $P_{\rm ext}=10^{5.5}~{\rm K~cm^{-3}}$, metallicity $10^{-2.00}~Z_{\odot}$, and irradiated by a G_0 of $10^{4.50}\langle G_0\rangle$.

can deviate from 1/3, which is why in practice we calculated the two integrals over $\Lambda(R)$, in Equations (1) and (2), numerically for each cloud.

We have now calculated the correction factor that converts $I_{\text{int,slab}}$ into $I_{\text{int,pyra}}$, by comparing the integrals of Equations (1) and (2). We will assume that the same factor can be used to convert $I_{\text{em,slab}}$ to $I_{\text{em,pyra}}$ as well, which is expected to be a very good approximation in the case of optically thin emission, which is the case for most of the cloud models used in this work. The resulting geometrical correction factor ranges from 0.08 to 0.92 in our default grids of cloud models. Figure 2 shows $\Lambda(R)$ as a function of R in the cloud with these extreme correction factors. Both clouds happen to be GMCs (not diffuse gas clouds), and the different radial profiles of $\Lambda(R)$ result in very different correction factors.

Figure 3 shows histograms of the correction factors to the [C II] emission for all three ISM phases in all model galaxies. These correction factors were calculated by interpolating in the grid of CLOUDY models for each gas cloud. In the case of GMCs and diffuse ionized gas clouds, there is a tail of clouds with correction factors below the minimum value of 0.08 quoted above, due to the interpolation method used to get gas cloud properties in the galaxy from the grids of cloudy models.

3. Updated Results

Adopting the emergent intensity, scaled by the geometrical correction factor and accounting for the CMB, results in the published line luminosities decrease by, on average, about 30% in [C II], 60% in [O I], and 47% in [O III] with default assumptions. See Table 1 for exact values of the line luminosities, both original and corrected. For the [C II] and [O III] emission, this decrease is caused mainly by a decreased line luminosity of the diffuse gas. For the [O I] emission, this decrease is caused by a decreased line luminosity of the GMCs (which are also in the brightest ISM phase in [O I]). This makes the GMCs the most [C II] luminous ISM phase (see Figure 7 below), except in galaxies with high SFR surface density in which the [C II] luminosity of the diffuse gas is not nearly as affected by the CMB. Figures 6–11 and 14 are affected by this correction and updated versions can be found below.

The revised [C II] contributing fractions above are in better agreement with other works on the same topic and observations of the Milky Way. Vallini et al. (2015) derive a [C II] contribution from PDRs associated with molecular gas of >90%, by far, the dominating [C II] source in their model galaxies at $z \approx 6.6$. Similarly, Pallottini et al. (2017) find that >95% of the [C II] luminosity comes from dense gas in the molecular disk of their z = 6 model galaxy. In our Milky Way, dense PDRs and CO-dark H2 gas are also dominant [C II] emitters, responsible for about \sim 55% of the total [C II] emission, while the diffuse ionized gas and diffuse neutral gas contribute \sim 20% and 25%, respectively (Pineda et al. 2014).

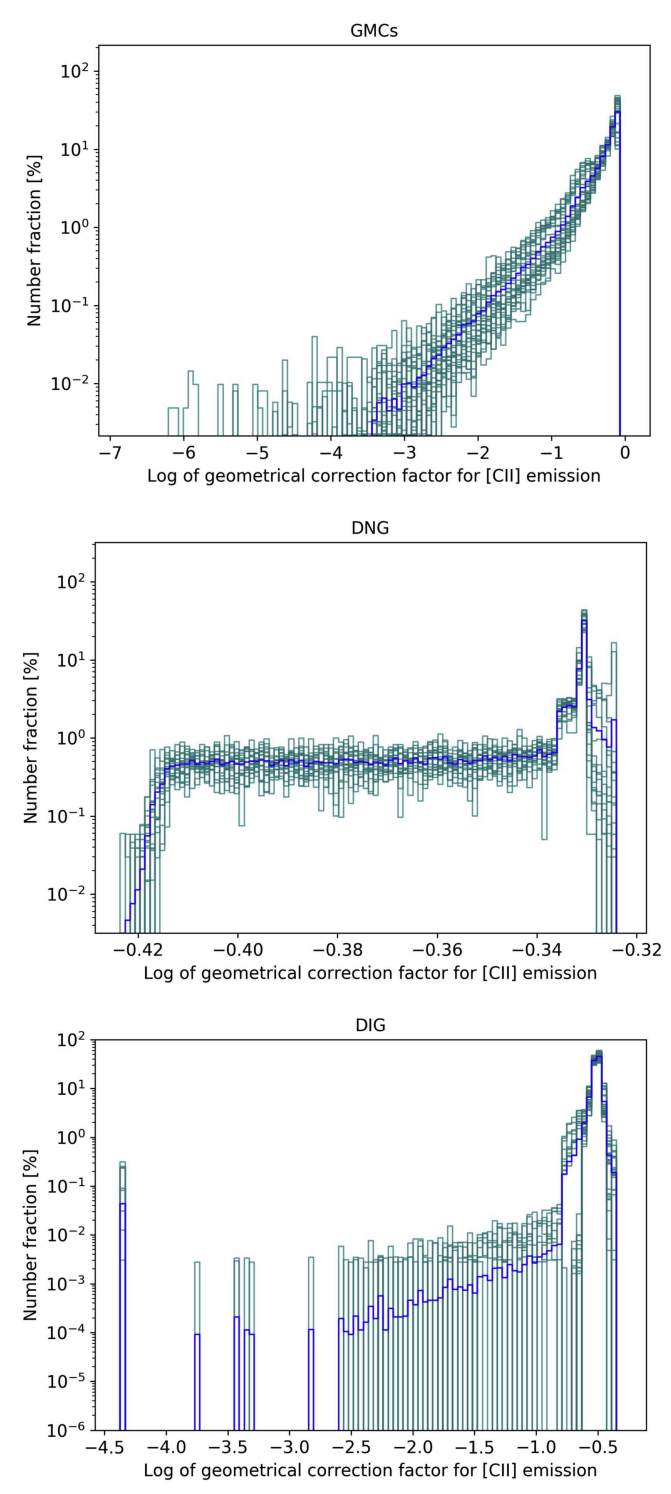


Figure 3. Histograms of the geometrical correction factors used for all model galaxies in GMCs (left), diffuse neutral gas (middle) and diffuse ionized gas (right), with the mean value shown in blue.

With the implementation of the correction described in the previous section, the new $L_{\text{IC II}}$ -SFR relation is

$$\log(L_{\rm [C II]}[L_{\odot}]) = (6.42 \pm 0.10) + (0.68 \pm 0.08) \times \log(SFR[M_{\odot} \text{ yr}^{-1}]). \tag{6}$$

The rms scatter of the simulated galaxies around this relation is 0.07 dex. The slope does not change significantly, but the intercept is decreased substantially from the original relation in the paper.

In Section 4.2 of the paper, the corrected [C II] luminosity fractions are \sim 5%-86% (average \sim 50%) for the GMCs, \sim 0.4%-25% (average \sim 6%) for the diffuse neutral gas, and \sim 13%-89% (average \sim 44%) for the diffuse ionized gas. This changes the picture painted in the original paper about which ISM phase dominates the [C II] emission at $z \sim$ 6. We now find that the [C II] emission is dominated by the molecular clouds more than by the diffuse ionized gas, with, on average, \sim 50% and \sim 44% each, respectively. The

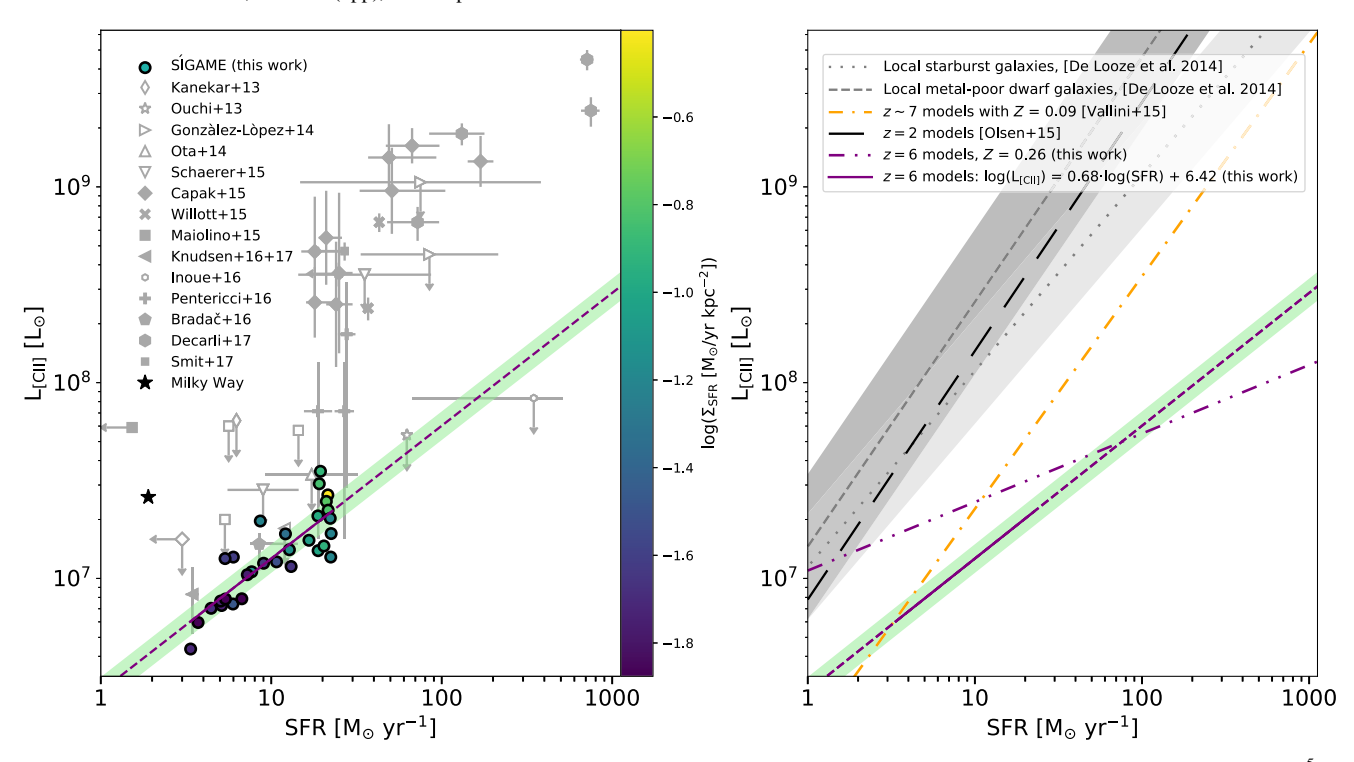


Figure 6. Left: the [C II] luminosity vs. SFR. For the sake of clarity, we have not included MS0451-H (z=6.703) in the plot. This source has $L_{\rm [C II]} < 3 \times 10^5 \, L_{\odot}$ and SFR $\sim 0.4 \, M_{\odot} \, {\rm yr}^{-1}$ (Knudsen et al. 2017) and lies about 1 dex below our fitted relation. All SFRs have been converted to a Chabrier IMF where applicable. Right: a comparison with other, observed and simulated, [C II]–SFR relations. Shown are the [C II]–SFR relations derived by De Looze et al. (2014) for local metal-poor dwarf galaxies (gray dashed line) and local starburst galaxies (gray dotted line); gray dashed and dotted lines, respectively, with the shaded regions indicating the rms scatter of these relations). Also shown are simulated relations of z=2 main-sequence galaxies (black long dashed line; Olsen et al. 2015) and $z\sim7$ galaxies (orange dashed–dotted line; Vallini et al. 2015).

Table 1
Derived Line Luminosities for the 30 Simulated $z \simeq 6$ Galaxies Used for This Work, with Both Original and New Corrected Values Shown

Name	$L_{ m [CII]}$ Original (10^6L_{\odot})	$L_{ m [C~II]}$ Corrected (10^6L_{\odot})	$L_{ m [OI]}$ Original (10^6L_{\odot})	$L_{\mathrm{[OI]}}$ Corrected (10 ⁶ L_{\odot})	$L_{ m [O~III]}$ Original (10^6L_{\odot})	$L_{ m [O~III]}$ Corrected (10 ⁶ L_{\odot})
G1	8.85	5.96	68.41	32.49	12.08	4.43
G2	6.23	4.36	74.53	44.94	6.19	2.30
G3	10.66	7.04	119.46	47.60	11.68	4.67
G4	11.44	7.27	207.53	84.45	10.95	4.00
G5	20.22	12.85	461.09	169.75	13.52	6.10
G6	10.00	7.40	191.85	92.80	13.29	4.21
G7	12.58	7.66	324.42	110.47	10.09	4.00
G8	11.88	7.85	165.06	80.87	11.06	4.42
G9	17.48	12.63	166.28	81.95	13.36	5.28
G10	14.21	10.81	424.52	213.15	18.69	17.64
G11	12.69	7.87	178.07	66.60	16.84	5.87
G12	24.81	10.45	276.15	70.66	18.34	9.01
G13	18.56	14.01	185.61	78.43	28.07	25.80
G14	17.95	11.95	272.50	112.68	15.77	6.39
G15	35.13	16.89	453.83	147.74	48.16	13.25
G16	19.51	15.66	373.90	167.79	28.74	24.72
G17	23.73	19.64	276.85	152.07	17.82	5.55
G18	26.70	11.50	253.17	89.41	19.64	8.61
G19	28.74	12.16	157.25	59.86	15.56	7.88
G20	23.78	13.86	179.42	56.46	50.31	46.55
G21	22.71	26.70	359.18	129.75	186.28	94.42
G22	36.09	24.75	146.62	52.67	113.80	84.93
G23	32.76	22.32	282.86	81.50	101.08	74.40
G24	23.29	20.85	234.72	113.07	39.91	30.00
G25	54.85	35.25	235.02	85.26	124.71	106.55
G26	28.08	20.28	337.31	149.23	33.86	10.16
G27	23.95	16.95	199.06	77.61	38.57	11.63
G28	13.89	12.86	225.87	87.22	20.09	6.05
G29	15.31	14.65	253.36	115.15	19.71	13.84
G30	43.47	30.45	253.17	87.01	135.26	99.89

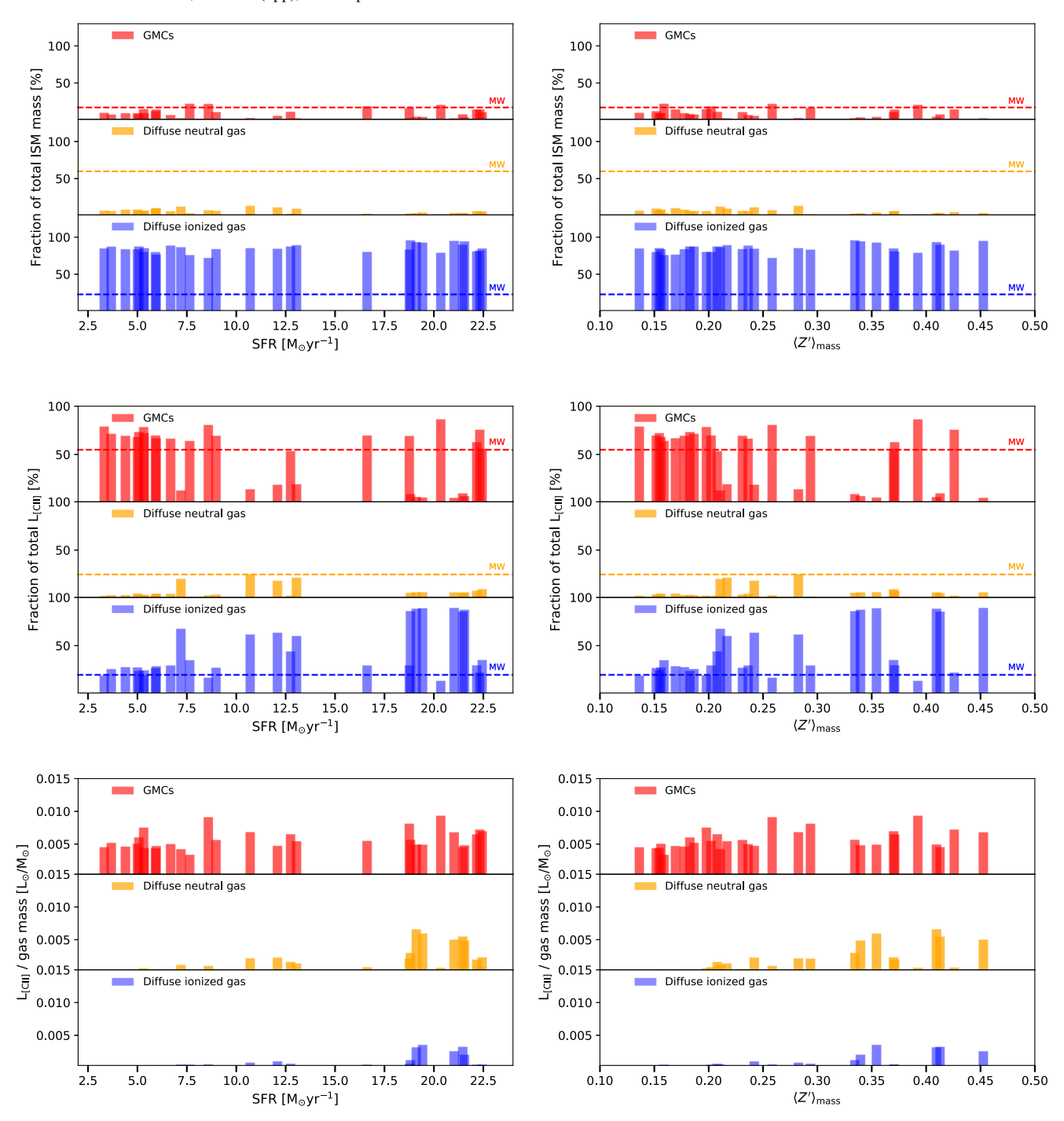


Figure 7. Top: mass fractions of the three ISM phases of our simulated galaxies as a function of their total SFRs (left panel) and mass-weighted average metallicities, $\langle Z \rangle_{mass}$ (right panel). The three ISM phases, GMCs, diffuse neutral gas, and diffuse ionized gas, are shown as red, orange, and blue shaded regions, respectively. The corresponding mass fractions in the MW have been shown with horizontal dashed lines: 17% H₂ (red), 60% H I (orange), and 23% H II (blue) within 20 kpc with numbers from Draine (2011). Middle: the contributions from the ISM phases to the total [C II] luminosities vs. SFRs (left panel) and $\langle Z \rangle_{mass}$ (right panel). The horizontal dashed lines indicate the corresponding fractions for the MW (Pineda et al. 2014). Bottom: the [C II] luminosity per gas mass of each ISM phase vs. SFRs (left panel) and $\langle Z \rangle_{mass}$ (right panel).

[C II] emission in 20 out of 30 galaxies is dominated by molecular gas, and by diffuse ionized gas in the rest. In Section 4.3, Equation (7) now reads

$$\log(L_{\text{[O III]}}[L_{\odot}]) = (5.68 \pm 0.19) + (1.38 \pm 0.23) \times \log(\text{SFR}[M_{\odot} \text{ yr}^{-1}]). \tag{7}$$

In Section 4.4, the result of the PCA is slightly changed, affecting Equations (11)–(13):

$$\log(L_{\rm [C~II]}) = 7.12 - 0.12 \log({\rm SFR}) + 0.51 \log(\langle Z \rangle_{\rm SFR}) + 0.49 \log(\Sigma_{\rm SFR}) + 0.70 \log(M_{\rm ISM}), \tag{11}$$

$$\log(L_{\rm [C II]}) = 7.12 + 0.26\log({\rm SFR}) + 0.26\log({\rm SFR}) + 0.24\log(\langle Z \rangle_{\rm SFR}) - 0.02\log(\Sigma_{\rm SFR}), \tag{12}$$

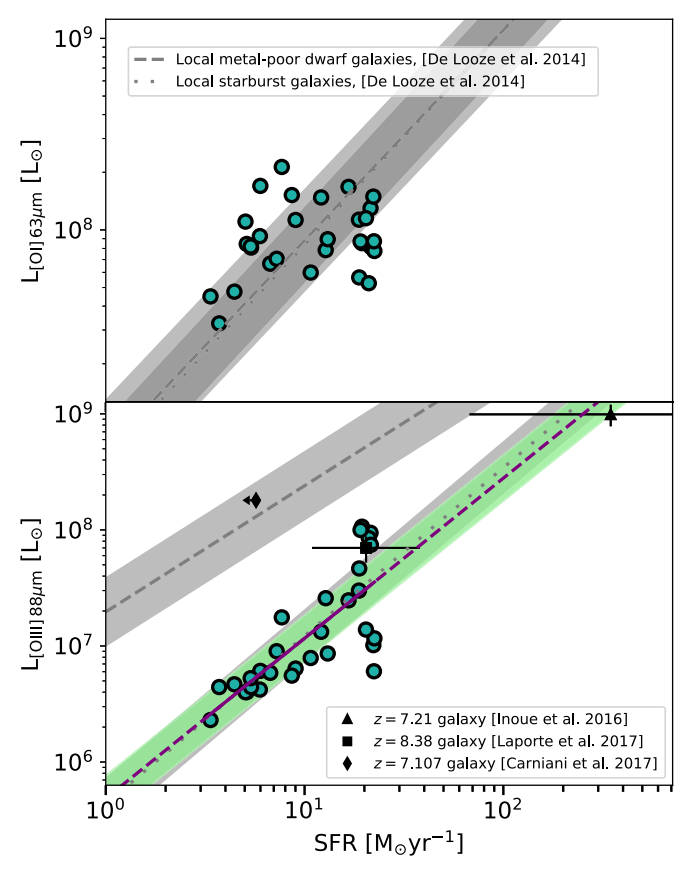


Figure 8. $L_{\rm [O\,II]}$ vs. SFR (top) and $L_{\rm [O\,III]}$ vs. SFR (bottom) for our simulated galaxies (filled circles) compared to $z\gtrsim 5$ observations of the two lines. A log-linear fit to the [O III] simulations is shown by the purple dashed line with a 1σ scatter (0.15 dex) in $L_{\rm [O\,III]}$ as indicated by the green shaded region. Local relations for metal-poor dwarf galaxies (gray dashed lines) and local starburst galaxies (gray dotted lines) are shown for comparison (De Looze et al. 2014). The gray-shaded regions indicate the $\pm 1\sigma$ scatter around these relations. Also shown are the detections to date of [O III] in star-forming galaxies at $z\gtrsim 5$ (Inoue et al. 2016; Carniani et al. 2017; Laporte et al. 2017).

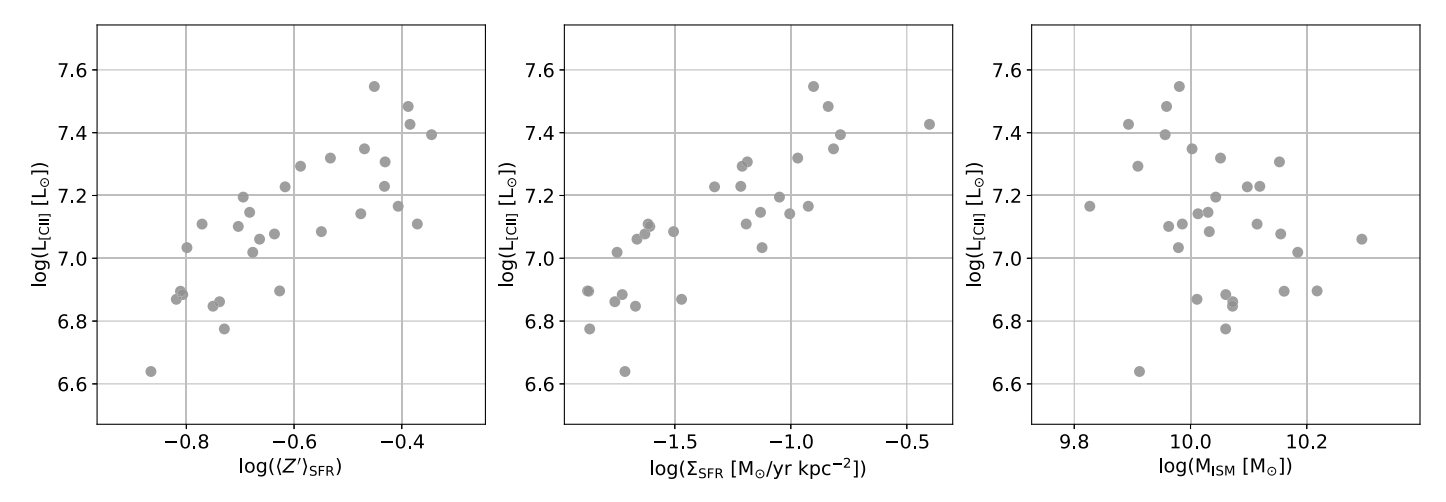


Figure 9. $L_{\rm [C\ II]}$ vs. $\langle Z \rangle_{\rm SFR}$ (left), $\Sigma_{\rm SFR}$ (middle), and $M_{\rm ISM}$ (right) for simulated galaxies.

$$\log(L_{\rm [C II]}) = 7.12 + 0.53 \log(SFR) + 0.28 \log(\langle Z \rangle_{SFR}). \tag{13}$$

The authors acknowledge Dr. Guilaine Lagache for her insightful comments and questions that led us to the discovery of this error. The authors also thank the referee deeply for having returned to our work and read the manuscript in detail. This work benefited from resources provided by the NASA High-End Computing (HEC) Program through the NASA Advanced Supercomputing (NAS) Division.

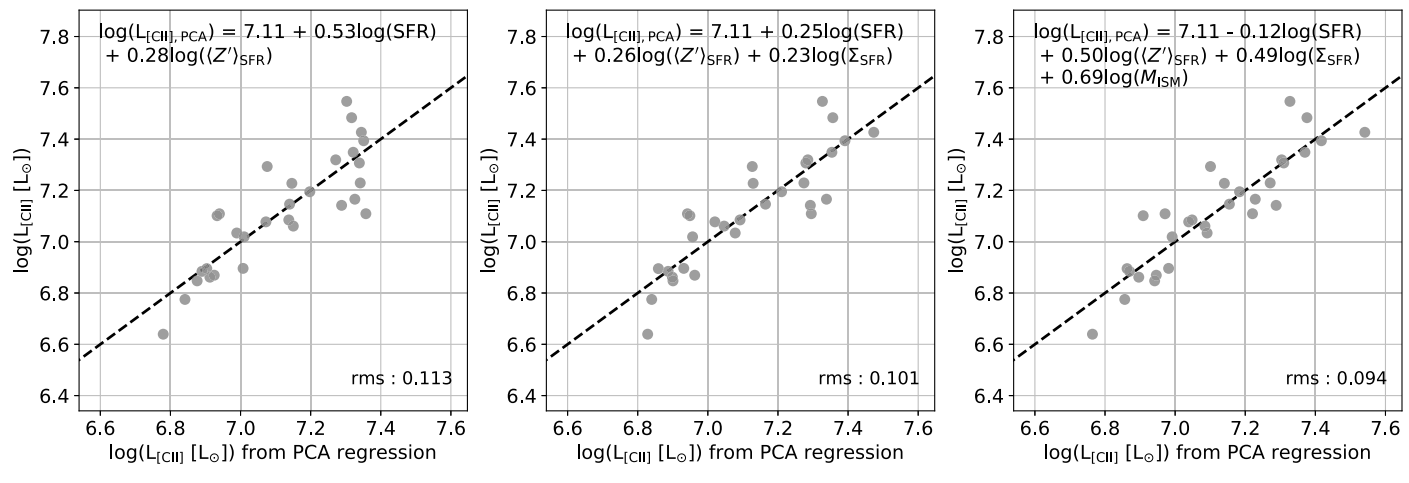


Figure 10. Results of a PCA regression to the [C II] luminosities of our simulations using different sets of free parameters. Left panel: SFR and $\langle Z \rangle_{SFR}$ (see Equation (13) in the published article). Middle panel: SFR, $\langle Z \rangle_{SFR}$ and Σ_{SFR} and Σ_{SFR} (see Equation (12) in the published article). Right panel: SFR, Σ_{SFR} and Σ_{SFR} (see Equation (11) in the published article). The dashed lines indicate the 1:1 line. The rms scatter of the simulations with respect to Equations (11)–(13) in the published article is indicated.

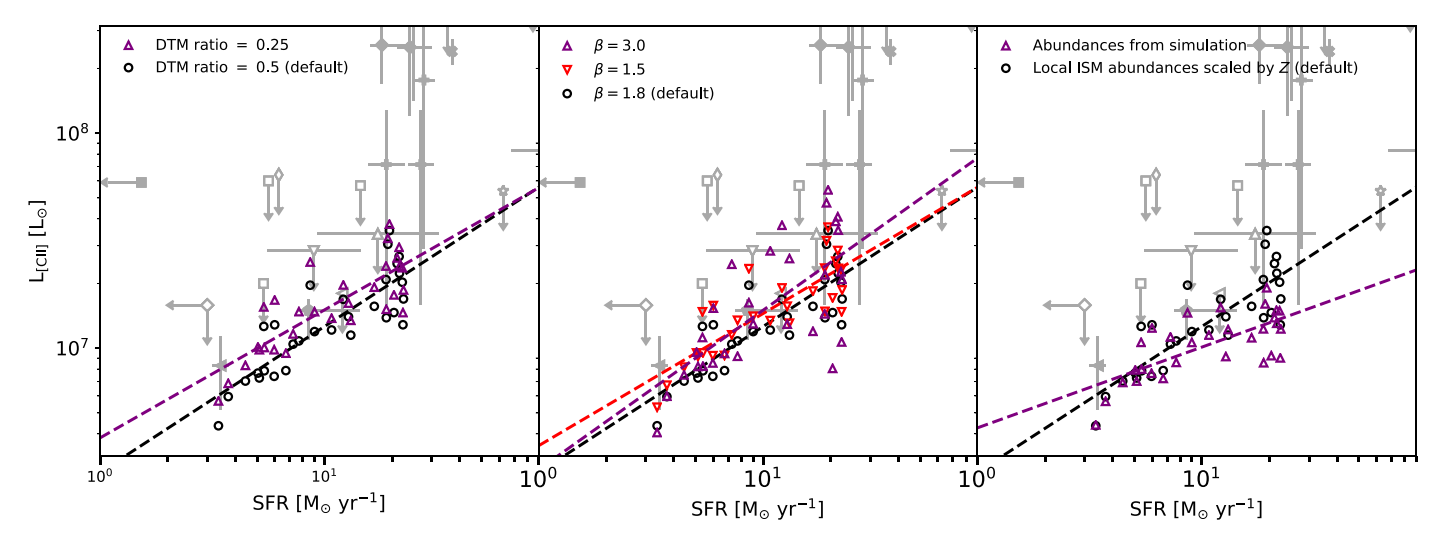


Figure 11. Result of deviating from the default assumptions of SÍGAME. Purple triangles show the simulated galaxies in the $L_{[CII]}$ -SFR diagram after reducing the DTM ratio by a factor of 2 (left); changing the GMC mass spectrum to one that is more bottom- or top-heavy (middle); adopting abundances that better match the cosmological simulation (right). Black circles show the location of model galaxies with the default assumptions of SÍGAME. Observations are shown with gray symbols, as in Figure 6.

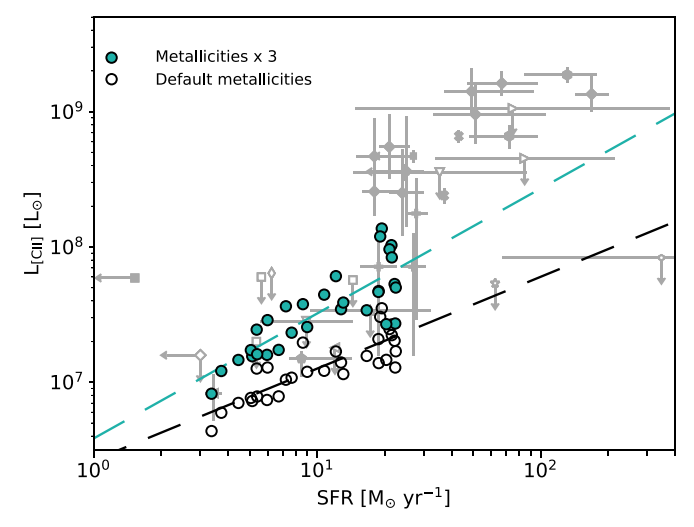


Figure 14. Effect of boosting the (default) metallicities of each fluid element in our simulations by a factor of three results in galaxy [C II] luminosities (filled cyan circles) that are on average ~ 2.5 –3× higher. Even so, this does not bring the simulations fully into accord with the [C II]-bright detections at $z \simeq 6$, although there is an overlap with observations for some simulations. The dashed cyan line shows the log-linear fit to the simulations with high metallicities.

ORCID iDs

References

Carniani, S., Maiolino, R., Pallottini, A., et al. 2017, A&A, 605, 42
Chatzikos, M., Ferland, G. J., Williams, R. J. R., Porter, R., & van Hoof, P. A. M. 2013, ApJ, 779, 122
De Looze, I., Cormier, D., Lebouteiller, V., et al. 2014, A&A, 568, A62
Draine, B. T. 2011, Physics of the Interstellar and Intergalactic Medium (Princeton, NJ: Princeton Univ. Press)
Inoue, A. K., Tamura, Y., Matsuo, H., et al. 2016, Sci, 352, 1559
Knudsen, K. K., Watson, D., Frayer, D., et al. 2017, MNRAS, 466, 138

Laporte, N., Ellis, R. S., Boone, F., et al. 2017, ApJL, 837, L21
Olsen, K. P., Greve, T. R., Narayanan, D., et al. 2015, ApJ, 814, 76
Pallottini, A., Ferrara, A., Gallerani, S., et al. 2017, MNRAS, 465, 2540
Pineda, J. L., Langer, W. D., & Goldsmith, P. F. 2014, A&A, 570, A121
Vallini, L., Gallerani, S., Ferrara, A., Pallottini, A., & Yue, B. 2015, ApJ, 813, 36